Structural Evidence for Common Ancestry of the Nuclear Pore Complex and Vesicle Coats
Stephen G. Brohawn, *et al.*
Science **322**, 1369 (2008);
DOI: 10.1126/science.1165886

Structural Evidence for Common Ancestry of the Nuclear Pore Complex and Vesicle Coats

Stephen G. Brohawn,[1]* Nina C. Leksa,[1]* Eric D. Spear,[1]
Kanagalaghatta R. Rajashankar,[2] Thomas U. Schwartz[1]†

Nuclear pore complexes (NPCs) facilitate nucleocytoplasmic transport. These massive assemblies comprise an eightfold symmetric scaffold of architectural proteins and central-channel phenylalanine-glycine-repeat proteins forming the transport barrier. We determined the nucleoporin 85 (Nup85)•Seh1 structure, a module in the heptameric Nup84 complex, at 3.5 angstroms resolution. Structural, biochemical, and genetic analyses position the Nup84 complex in two peripheral NPC rings. We establish a conserved tripartite element, the ancestral coatomer element ACE1, that reoccurs in several nucleoporins and vesicle coat proteins, providing structural evidence of coevolution from a common ancestor. We identified interactions that define the organization of the Nup84 complex on the basis of comparison with vesicle coats and confirmed the sites by mutagenesis. We propose that the NPC scaffold, like vesicle coats, is composed of polygons with vertices and edges forming a membrane-proximal lattice that provides docking sites for additional nucleoporins.

Exchange of macromolecules across the nuclear envelope is exclusively mediated by NPCs (*1*–*3*). Whereas much progress has been made understanding the soluble factors mediating nucleocytoplasmic transport, the structure of the ~40- to 60-MD NPC itself is still largely enigmatic. Cryo-electron tomography (cryo-ET) and cryo-electron microscopy (cryo-EM) have established the NPC structure at low resolution (*4*–*6*). Crystal structures of scaffold NPC components are emerging (*7*–*10*), but the resolution gap still precludes fitting into the cryo-ET structure. Overall, the NPC has eightfold rotational symmetry with an outer diameter of ~100 nm and a core scaffold ring ~30 nm wide. The central FG repeat containing transport channel measures ~40 nm in diameter, defining the maximum size of substrates (*11*).

The modularity of the NPC assembly suggests a path toward a high-resolution structure (*12*). Of the ~30 bona fide nucleoporins (Nups) that compose the NPC, only a core subset is stably attached (*13*). In *Saccharomyces cerevisiae*, this core includes two essential complexes: the heptameric Nup84 complex and the heteromeric Nic96-containing complex (hereafter called the Nic96 complex; unless noted, all proteins are from *S. cerevisiae*). The Nup84 complex is composed of one copy each of Nup84, Nup85, Nup120, Nup133, Nup145C, Sec13, and Seh1. It self-assembles from recombinant proteins in vitro and forms a branched Y-shaped structure (*14*). Deletion or depletion of individual components of the Nup84 complex leads to severe assembly defects in many organisms (*15*–*17*). The Nic96 complex is less well characterized but appears to contain the architectural nucleoporins Nup157/170, Nup188, Nup192, Nup53, and Nup59 (*18*–*20*). β propellers and stacked α-helical domains form the building blocks of the constituents of Nup84 and Nic96 complexes (*12*, *21*). Because vesicle coats [including coat protein complex I (COPI), COPII, and clathrin] share similar elements, a common ancestry has been hypothesized despite very low sequence homology and the absence of experimental structural evidence (*22*).

A recent computer-generated model of the NPC based on a plethora of primary data from different sources placed the Nup84 complex at the NPC periphery, sandwiching the Nic96 complex in the center (*23*). In contrast, a model solely based on the structure of the Nup145C•Sec13 heterodimer and crystal packing interactions was proposed that is inconsistent with the computer model (*9*).

We solved the structure of a complex of Nup85 residues 1 to 564 (of 744) and intact Seh1 (referred to as Nup85•Seh1) at 3.5 Å (table S1). Seh1 and Nup85 form distinct units in a tightly associated complex (Fig. 1 and fig. S1). Seh1 folds into an open six-bladed β-propeller structure. The blades fan out consecutively around a central axis, typical for canonical β-propeller structures (*24*). Between blades 1 and 6, the N terminus of Nup85 is inserted and forms a three-stranded blade that completes the Seh1 propeller in trans. Following its N-terminal insertion blade, Nup85 forms a compact cuboid structure composed of 20 helices, with two distinct modules, referred to as "crown" and "trunk." Helices α1 to α3 (residues 100 to 200) meander along one side of the trunk; the other side is formed by helices α12 to α19 (residues 362 to 509) running in the opposite direction in an antiparallel zigzag to the C terminus. The trunk elements are separated by an intervening crown composed of helices α4 to α11 (residues 201 to 361) that form a distinct bundle that caps one end of the trunk. Helices α5 to α10 in the crown module are almost perpendicular to the helices in the trunk.

In the asymmetric unit of the crystal, two heterodimers are aligned along a noncrystallographic dyad, generating patches of contacts (fig. S2). This interaction is unlikely to be functionally meaningful because the contact residues are poorly conserved in orthologs. Moreover, analysis of Nup85•Seh1 by analytical ultracentrifugation (AUC) showed a single species of ~104 kD with a hydrodynamic radius of 4.4 nm (fig. S3). This hydrodynamic radius is

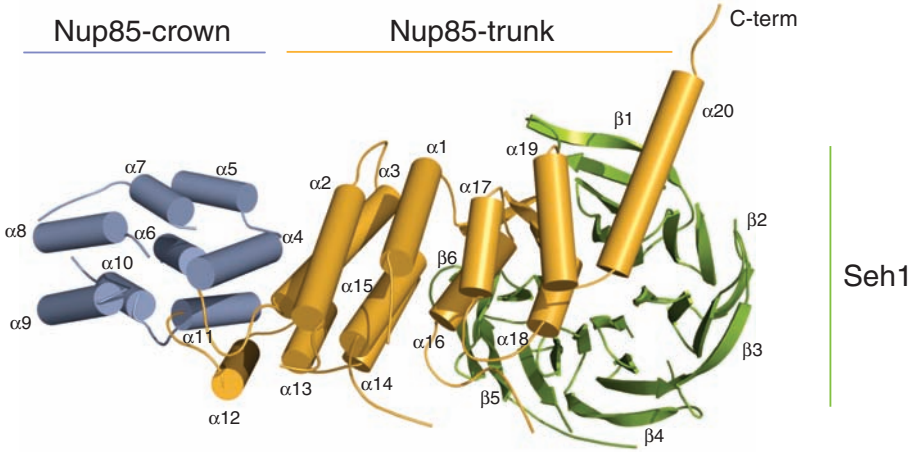

Fig. 1. Structure of the Nup85•Seh1 complex. The structure of the heterodimeric Nup85•Seh1 complex is shown. Nup85 has a trunk (orange, helices α1 to α3 and α12 to α20) and a crown (blue, helices α4 to α11) module. The β strands at the extreme N terminus of Nup85 form an insertion blade, which complete the Seh1 (green) β propeller.

[1]Department of Biology, Massachusetts Institute of Technology, 77 Massachusetts Avenue, Cambridge, MA 02139, USA. [2]Northeastern Collaborative Access Team, Building 436, Argonne National Laboratory, Argonne, IL 60439, USA.

*These authors contributed equally to this work.
†To whom correspondence should be addressed. E-mail: tus@mit.edu

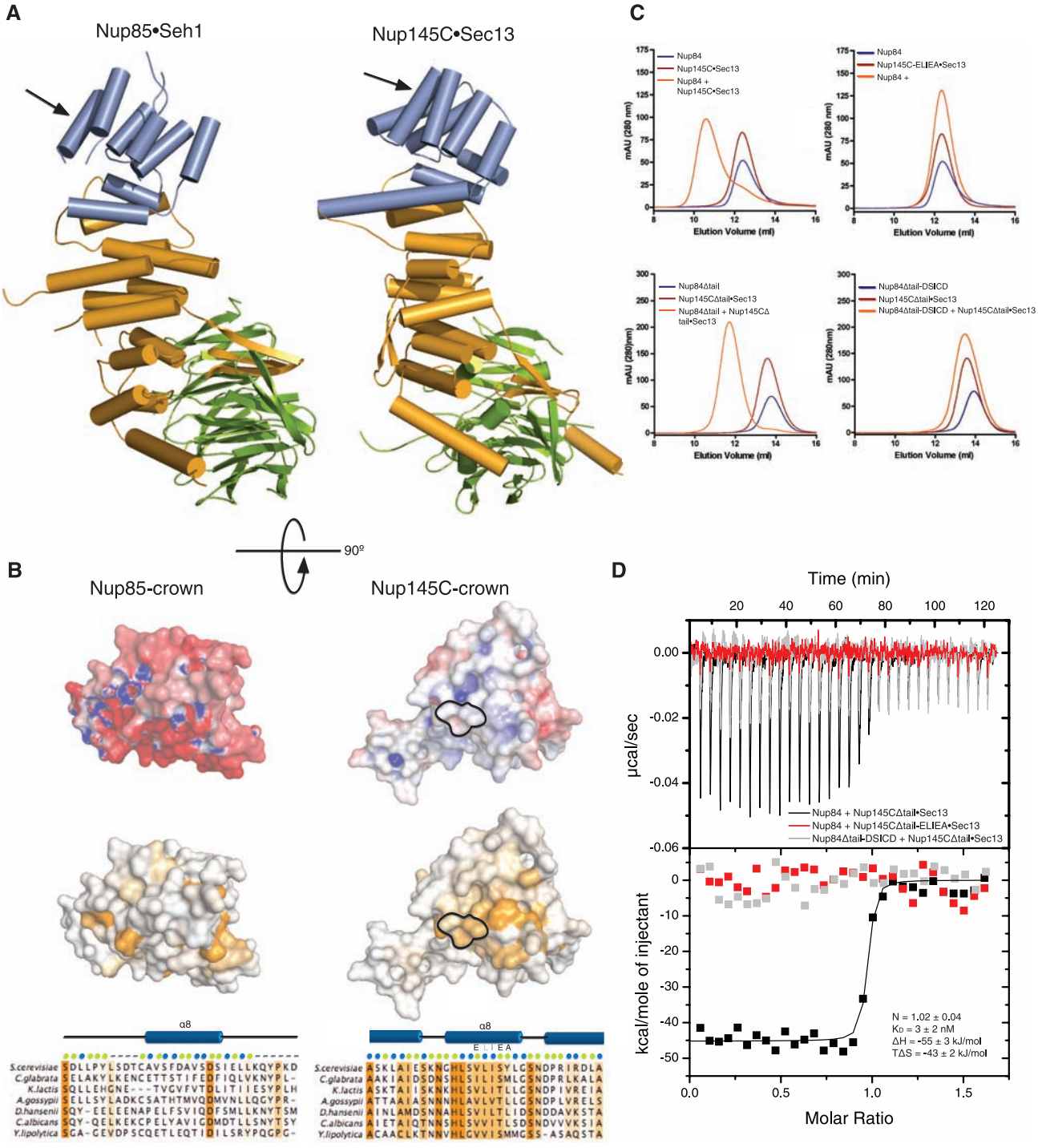

Fig. 2. Comparison of Nup85•Seh1 and Nup145C•Sec13 and identification of the Nup84•Nup145C crown-crown binding interface. (**A**) The topologies of the Nup85•Seh1 (left) and Nup145C•Sec13 [right, PDB code 3BG1 (*9*)] complexes are shown, illustrating an overall similarity with three shared structural elements: trunk, crown, and β propeller. Colors are assigned as in Fig. 1. (**B**) Surface representations of the crowns of Nup85 and Nup145C are shown colored according to electrostatic surface potentials (top) and sequence conservation (bottom) in a view rotated 90° from (A). Sequence conservation has its basis in the phylogenetic tree of budding yeasts (*40*) and is colored from white (not conserved) to orange (conserved). A partial sequence alignment of helix α8 [indicated by arrows in (A)] is also shown, with surface-exposed residues indicated by green dots, residues buried in the hydrophobic core by blue dots, and residues not modeled in the structure by dashes (*26*). Mutations made in this helix in Nup145C are shown above the sequence alignment, and the corresponding residues are outlined in the surface representations of Nup145C. (**C**) In the top graphs, gel filtration data of Nup84 alone, Nup145C•Sec13 (wild type or -ELIEA mutant) alone, and Nup84 plus Nup145C•Sec13 (wild type or -ELIEA mutant) are shown. The shift in the Nup84 plus wild-type Nup145C•Sec13 chromatogram indicates complex formation and is absent in the case of the -ELIEA mutant. In the bottom graphs, gel filtration data of Nup145C•Sec13 alone, Nup84 alone (wild type or -DSICD mutant) alone, and Nup145C•Sec13 plus Nup84 (wild type or -DSICD mutant) are shown. The shift in the Nup145C•Sec13 plus wild-type Nup84 chromatogram indicates complex formation and is absent in the case of the -DSICD mutant. (**D**) ITC data illustrating high-affinity binding for wild-type Nup145C•Sec13 and Nup84 (black). Experimental values for N, K_d, enthalpy ΔH, and entropy $T\Delta S$ are shown. In contrast, binding is lost for both crown-surface mutants Nup84-DSICD (gray) and Nup145C-ELIEA (red).

close to the theoretical value calculated from the atomic coordinates with use of HYDROPRO (*25*) and reflects the elongated shape of the 103-kD Nup85•Seh1 complex (a spherical protein of 220 kD would have the same radius). Gel filtration also showed that Nup85•Seh1 is a single 103-kD heterodimer at concentrations up to 20 mg/ml (fig. S4). Hence, we restrict our analysis to this heterodimer.

The connectivity and topology of secondary structure elements and the three-dimensional folds of Nup85•Seh1 and Nup145C•Sec13 (*9*) are remarkably similar (Fig. 2A), despite very low sequence identity between Nup85 and Nup145C (10%) and moderate identity between Seh1 and Sec13 (32%). Like Nup85, Nup145C has an N-terminal three-stranded β sheet that provides a seventh blade to close the open β propeller of Sec13. The trunk and crown modules of Nup145C are also similar to those in Nup85, although their relative orientation is modestly different in the two proteins.

The most conserved regions of Nup85 are involved in the interaction with Seh1. The corresponding interface between Nup145C and Sec13 is also well conserved, but Nup145C has an additional highly conserved surface on the crown module around helix α8 that is not observed in Nup85 (Fig. 2B). This region is reasonably polar and poorly conserved in Nup85 but highly conserved and distinctly hydrophobic in Nup145C, suggesting a protein-protein interaction site. Nup84 and Nup120 bind to roughly opposite sides of Nup145C•Sec13 in the Y-shaped complex (*14*), and the C-terminal helical region of Nup145C is necessary for binding Nup120 (fig. S5). Thus, we hypothesized that the α8 crown surface of Nup145C is the binding site for Nup84.

To test this hypothesis, we mutated the Nup145C sequence VLISY (*26*) in α8 to ELIEA, introducing two negative charges and eliminating a conserved aromatic side chain on the crown surface (Fig. 2B). The overall structure of Nup145C did not appear to be perturbed by this modification: (i) Nup145C-ELIEA•Sec13 bound to Nup120 to form a 1:1 complex indistinguishable from one formed with Nup145C•Sec13 in gel-filtration experiments (fig. S6); Nup145C•Sec13 and Nup145C-ELIEA•Sec13 complexes (ii) had comparable thermostability (fig. S7) and (iii) showed identical behavior in gel filtration (Fig. 2C). The ELIEA mutation completely eliminated Nup84 binding. In isothermal-titration calorimetry (ITC) experiments, Nup84 bound wild-type Nup145C•Sec13 tightly [dissociation constant (K_d) = 3 ± 2 nM; 1:1 stoichiometry] but not Nup145C-ELIEA•Sec13 (Fig. 2D). Similarly, Nup84 formed a stable complex with Nup145C•Sec13 but not with Nup145C-ELIEA•Sec13 in gel filtration (Fig. 2C). We conclude that the Nup84 binding site on Nup145C includes the exposed surface of helix α8.

To determine the consequences of abolishing the Nup84 binding site on Nup145C in vivo, we introduced the Nup145C-ELIEA mutation into the *NUP145* gene in yeast. Strains carrying *NUP145-ELIEA* in a Δ*NUP145*/*NUP84-GFP* or Δ*NUP145*/*NUP133-GFP* background displayed a marked defect in incorporating Nup84–green fluorescent protein (GFP) and Nup133-GFP into the NPC (Fig. 3 and fig. S8). Compared with wild type, a significantly larger fraction of GFP-tagged proteins was found in the cytoplasm, indicating that the Nup84 binding interface on Nup145C is crucial in recruiting both Nup133 and Nup84 to the NPC (fig. S10). In addition, nuclear pores were clustered into discrete foci on the nuclear envelope of the strains expressing Nup145C-ELIEA, indicative of severe NPC assembly defects and similar to Nup84 and Nup133 null strains (*27*, *28*). Cells expressing wild-type Nup145C demonstrated the expected punctate nuclear rim staining in both Nup84-GFP and Nup133-GFP strains. Thus, disruption of the Nup84 binding site on Nup145C affects NPC assembly and function and causes loss of Nup84 and Nup133 from pores. The loss of Nup133 can be rationalized because it is attached to the Y-shaped Nup84 complex through a binary interaction with Nup84 (*8*, *14*). Some Nup84 and Nup133 proteins remain associated with nuclear pores in the Nup145C-ELIEA expressing strains, arguing for the existence of additional weaker attachment sites for both proteins in the NPC. It has been shown that an ALPS membrane-binding motif is present in Nup133 (*29*). Because Nup133 and Nup84 are tightly associated (*8*), the ALPS motif might be weakly functional in recruiting Nup133•Nup84 to the NPC even when the Nup84•Nup145C interaction is compromised.

On the basis of lattice packing observed in crystals of Nup145C•Sec13, Hsia *et al*. (*9*) proposed that Nup145C•Sec13 and Nup85•Seh1 each form heterooctameric poles that span the entire NPC in a "concentric cylinder" model of NPC structure. However, the Nup145C•Sec13 lattice contacts involved in the putative heterooctamer overlap with the crown surface of Nup145C shown here to be the Nup84-binding site. Additionally, Nup145C•Sec13 and Nup85•Seh1 behave nearly identically during gel filtration, indicative of heterodimers when their large hydrodynamic radii are taken into account (Fig. 2 and fig. S4). AUC experiments confirmed that Nup85•Seh1 is a heterodimer in solution (fig. S3). Thus, the heterooctameric pole model (*9*) is inconsistent with our results.

The structural similarity between Nup85 and Nup145C extends to at least three other proteins (Fig. 4 and fig. S11). First, the architectural nucleoporin Nic96 (*10*) shares a common structural core (fig. S11) but has a distinct N terminus (Fig. 4). The shared cores mutually superimpose with a root mean square deviation of 3.0 to 3.5 Å. Nic96 has a trunk module (α1 to α3 and α12 to α19), a crown module (α4 to α11), and an N-terminal coiled-coil extension (instead of the insertion blade of Nup145C and Nup85) that tethers it to the FG-containing Nsp1 complex (*30*). Apart from the N-terminal differences, the three proteins differ mainly in the relative orientation of the crown and trunk modules. Although a previous comparison of Nup145C to the COPII coat component Sec31 did not reveal a strong similarity (*9*), comparison with Nup85, Nup145C, and Nic96 shows that Sec31 has corresponding trunk (α1 to α3 and α12 to α18) and crown (α4 to α11) modules. Sec31 homodimerizes to create an "edge element" in the COPII coat by an internal domain swap between two crown modules (*31*). This domain swap results in a mixed crown module that is identical in topology to the unmixed crowns in Nup85, Nup145C, and Nic96 (*31*). Structural prediction using Phyre (*32*) also places Nup84 in the group containing Nic96, Nup85, Nup145C, and Sec31. Similarity extends beyond the trunk and crown modules to a "tail" module that has been structurally characterized in the C-terminal domain of human Nup107 (homolog of yNup84) and in Nic96 (*8*, *10*) (fig. S11C). The

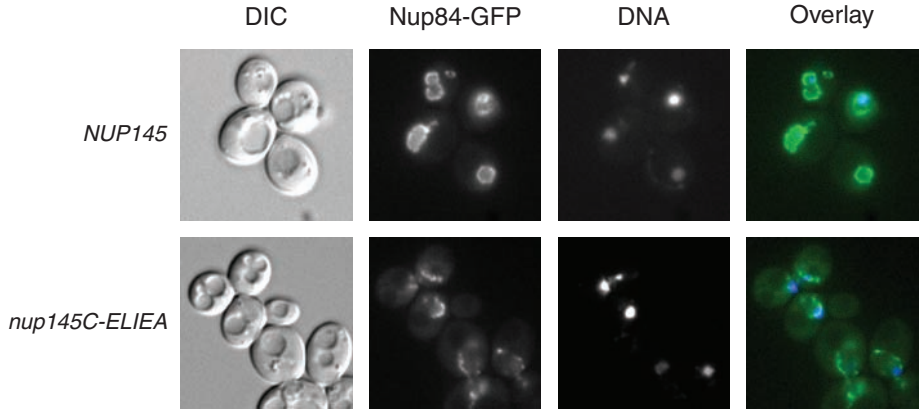

Fig. 3. Elimination of the Nup84 binding site on Nup145C results in nuclear pore assembly defects in vivo. *NUP145/NUP84-GFP* and *NUP145-ELIEA/NUP84-GFP* were grown at 24°C and visualized by fluorescence microscopy. Differential interference contrast, GFP-fluorescence, DNA (visualized with Hoechst dye), and false-colored overlay (GFP fluorescence is green, DNA blue) images of the same field are shown in columns from left to right.

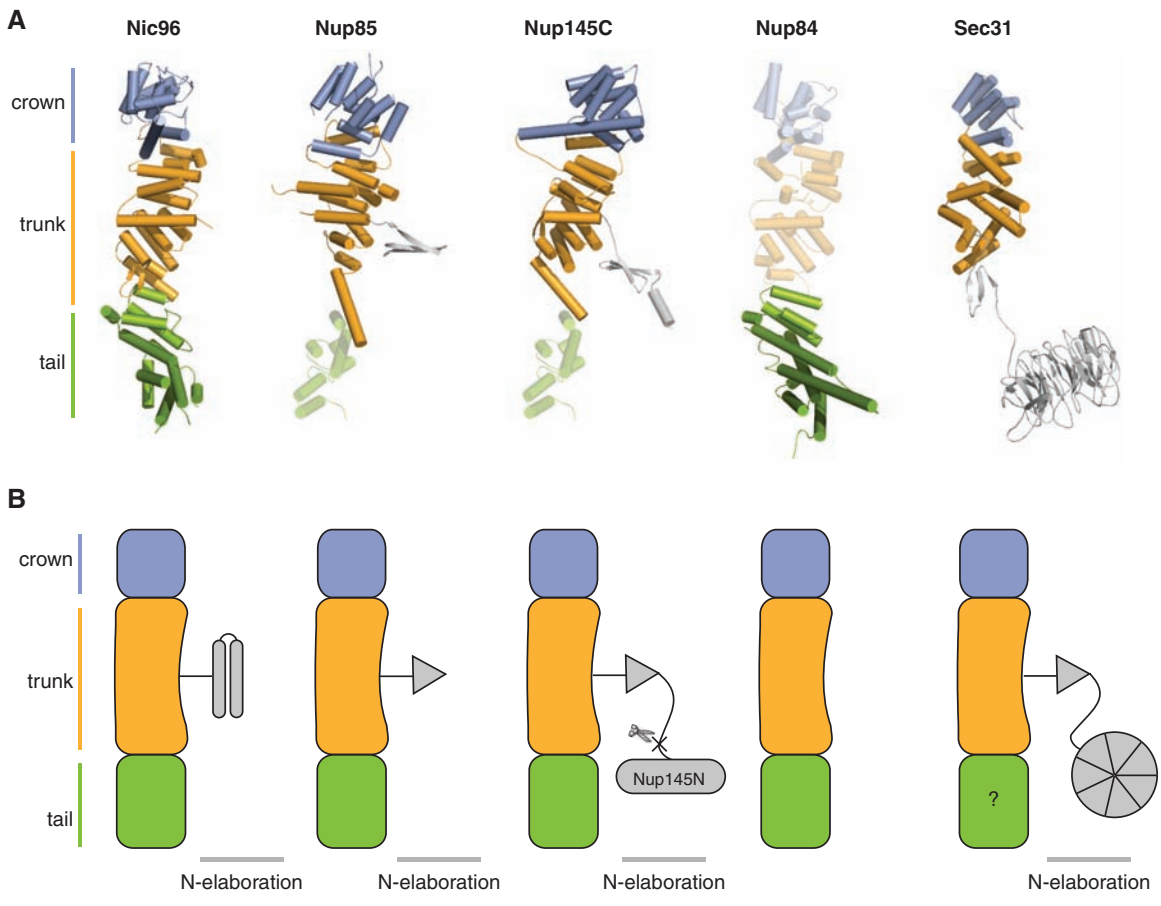

Fig. 4. Architecture of ACE1. (**A**) ACE1 containing proteins are shown as cylinders and sheets. Crowns are shown in blue, trunks in orange, tails in green, and other domains in gray. Modules with predicted structures are shown half-transparent. [PDB codes are 2QX5 for Nic96; 3BG1, Nup145C; 3CQC, Nup107 (Nup84 homolog); and 2PM6, Sec31] (**B**) Cartoons illustrating the similarity and modular nature of the ACE1 element. The N-terminal elaborations are, for Nic96, a coiled-coil domain that interacts with the Nsp1 complex; for Nup85, the Seh1-interacting insertion blade; for Nup145C, the Sec13-interacting insertion blade preceded by an autocatalytic cleavage domain and Nup145N; and, for Sec31, the Sec13-interacting insertion blade is preceded by its own N-terminal seven-bladed β propeller. Sec31 has a unique proline-rich insertion C-terminal to its trunk module followed by a conserved region predicted to be α-helical.

last three helices in the tail module of Nup107 form the interaction site with Nup133 (*8*). In Nic96, this region is predicted to be a protein binding site as well (*10*). Because we find this characteristic tripartite structural element of crown, trunk, and tail in architectural proteins of the NPC and the COPII coat, we term it the ancestral coatomer element 1 (ACE1).

Can we predict ACE1 functional sites from established interactions? Analogy to Sec31 monomers in the COPII edge element suggests that Nup145C and Nup84 might interact crown to crown. On the basis of the Phyre model and structural alignment, we constructed a surface point mutant, replacing two conserved hydrophobic residues on helix α8 of the Nup84 crown with aspartate [Nup84-ISICM to Nup84-DSICD (*26*)] (figs. S7 and S12). Nup84-DSICD disrupts Nup145C binding in a manner analogous to that of Nup145C-ELIEA, severing Nup84 binding as shown by gel filtration and ITC (Fig. 2, C and D). Thus, the Nup84•Nup145C interface is a crown-crown interaction involving α8 helices as in Sec31 homodimerization. Additionally, we found that the tail modules of Nup145C and Nup85 are necessary for interaction with Nup120 in a manner analogous to the human Nup107 interaction site for human Nup133 (*8*) (figs. S5 and S6).

Here, we have shown that ACE1 is abundant in the two main scaffolding subcomplexes of the NPC. To date, Nic96 is the only ACE1 protein in which all three modules (crown, trunk, and tail) are structurally defined. In Nic96, the three modules form a continuous, rigid hydrophobic core (*10*, *33*). In the other four experimental structures, only a subset of the modules are present. We speculate that the three modules within ACE1 can allow hinge movements, used to different extents in specific family members.

ACE1 is different from regular α-helical repeat structures, including HEAT repeats and TPR repeats [as discussed in (*10*)]. The α-helical modules that compose ACE1 are distinctly irregular, most notably with elements that fold back onto themselves, forming a U-turn within the crown module. The trunk is composed of two zigzagging helical units running in opposite directions. We propose that this architecture confers rigidity to the trunk and thus distinguishes it from regular helical repeat structures that are often inherently flexible (*34*). As a consequence of the specific arrangement of the helices in ACE1, several helices in trunk and crown are encased by neighboring helices and thus have a characteristic hydrophobic character (typically helices α6 and α10). This pattern of hydrophobic helices may help to find additional ACE1 proteins. Several sequence elements, notably in the crown and at the predicted hinge regions, distinguish ACE1 from other α-helical domains (*10*). Nevertheless, these characteristics are subtle enough to remain undetected in typical primary sequence (i.e., BLAST) searches, and candidate proteins need to be examined using all available tools, including phylogeny and secondary and tertiary structure analysis.

On the basis of distance constraints and stoichiometric considerations, the heptameric Y-shaped Nup84 complex has been placed in two concentric eight-membered rings on the nucleoplasmic and cytoplasmic faces of the NPC (*23*). But how is it oriented, and how is it connected to the inner ring of the scaffold? Nup133 is anchored to the structural scaffold by its interaction with Nup84, positioning it at the periphery of the pore (*8*). Nup84 is the link between Nup133 and Nup145C. Thus, we position the extended arm of the Y composed of Nup145C•Sec13, Nup84, and Nup133 facing outward (Fig. 5). Excluding the Nup133•Nup84 pair, the remaining pentamer forms a roughly symmetrical triskelion that conceptually resembles the vertex elements that form polygonal cages in vesicle coats. EM analysis showed that the triskelion measures about 20 nm between the tips (*14*). An eight-membered ring of the

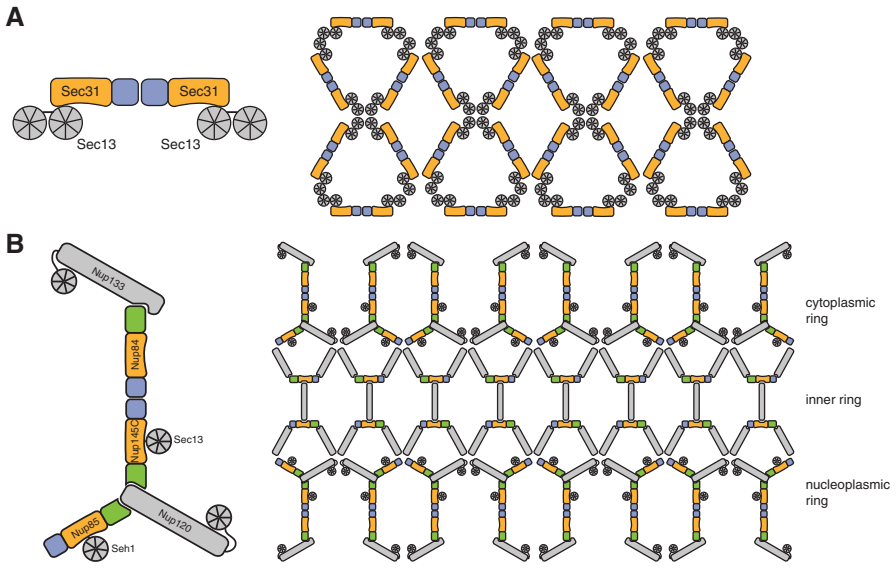

Fig. 5. Lattice model for the Nup84 complex and the structural scaffold of the NPC. The ACE1 proteins Nup85, Nup145C, Nup84, Sec31, and Nic96 are colored according to Fig. 4. (**A**) Schematic diagram of COPII outer coat organization. The Sec31•Sec13 cuboctahedron composed of 24 edge elements (Sec31•Sec13 heterotetramers) is shown unwrapped and laid flat in two dimensions. The Sec31•Sec31 crown-crown interactions make edge elements, whereas propeller-propeller interactions are vertex elements (*31*). (**B**) Schematic diagram of the predicted latticelike organization of the structural scaffold of the NPC. The entire scaffold (eight spokes) is illustrated unwrapped and laid flat in two dimensions. The Nup84 complex comprises the nuclear and cytoplasmic rings, whereas the Nic96-containing complex makes up the inner ring. The relative position and interactions between the seven proteins in the Nup84 complex are shown with Sec13, Seh1, Nup133, and Nup120 colored in gray. The remainder of the Nic96 complex (Nup157/170, Nup188, and Nup192) is illustrated in gray. The illustration is not meant to predict relative positions of proteins or structure of the inner ring per se but shows the latticelike organization of the structural scaffold that is similar to vesicle coating complexes.

Y complex around the central transport channel has an ~50-nm diameter if the edges were to touch at the tips. Alternatively, the Y complexes might connect through a yet-unidentified adaptor protein.

Two of the three interface types observed in the outer COPII coat are also found in the NPC coat (Fig. 5). Nup145C and Nup84 heterodimerize via their crown modules similar to Sec31 homodimerization, and the insertion of a seventh blade into an incomplete propeller domain is a recurring theme in Sec31•Sec13, Nup145C•Sec13, and Nup85•Seh1. Because Nic96 shares an ACE1 element, we predict that the inner scaffold ring is branched and latticelike, as are the peripheral rings. We postulate that the Nup84 and Nic96 complexes are both vertex elements in the assembly of the NPC structural scaffold. This would generate a latticelike NPC coat similar to clathrin and COP coats (*31*, *35*) (Fig. 5B). This model explains how the relatively small mass of Nup subcomplexes fills the large volume observed for the scaffold structure of the NPC (*23*) and is generally consistent with low-resolution images of NPCs (*4*, *6*). Notably, COP and clathrin cages do not directly contact membranes but use adaptor protein (AP) complexes to span the ~10-nm gap between the surfaces (*36*). Consistent with a related architecture, a similar sized gap has been observed between the scaffold ring and membrane surface in intact NPCs (*4*).

The modular nature of COP and clathrin coats enables the construction of assemblies varying in composition and size (*37*, *38*) because the polygonal elements can be arranged in different ways. If the same principle applies to the NPC, it could explain the existence of a subset of NPCs that do not obey eightfold rotational symmetry (*39*) or further allow for the assembly of NPCs of distinct composition, possibly tailored to more-specific tasks. These possibilities are now testable and will bring us closer to fully understanding the many functions of the NPC.

References and Notes

1. E. J. Tran, S. R. Wente, *Cell* **125**, 1041 (2006).
2. K. Weis, *Cell* **112**, 441 (2003).
3. M. A. D'Angelo, M. W. Hetzer, *Trends Cell Biol.* **18**, 456 (2008).
4. M. Beck, V. Lucic, F. Forster, W. Baumeister, O. Medalia, *Nature* **449**, 611 (2007).
5. S. P. Drummond, S. A. Rutherford, H. S. Sanderson, T. D. Allen, *Can. J. Physiol. Pharmacol.* **84**, 423 (2006).
6. D. Stoffler *et al.*, *J. Mol. Biol.* **328**, 119 (2003).
7. I. C. Berke, T. Boehmer, G. Blobel, T. U. Schwartz, *J. Cell Biol.* **167**, 591 (2004).
8. T. Boehmer, S. Jeudy, I. C. Berke, T. U. Schwartz, *Mol. Cell* **30**, 721 (2008).
9. K. C. Hsia, P. Stavropoulos, G. Blobel, A. Hoelz, *Cell* **131**, 1313 (2007).
10. S. Jeudy, T. U. Schwartz, *J. Biol. Chem.* **282**, 34904 (2007).
11. N. Pante, M. Kann, *Mol. Biol. Cell* **13**, 425 (2002).
12. T. U. Schwartz, *Curr. Opin. Struct. Biol.* **15**, 221 (2005).
13. G. Rabut, V. Doye, J. Ellenberg, *Nat. Cell Biol.* **6**, 1114 (2004).
14. M. Lutzmann, R. Kunze, A. Buerer, U. Aebi, E. Hurt, *EMBO J.* **21**, 387 (2002).
15. E. Fabre, E. Hurt, *Annu. Rev. Genet.* **31**, 277 (1997).
16. V. Galy, I. W. Mattaj, P. Askjaer, *Mol. Biol. Cell* **14**, 5104 (2003).
17. A. Harel *et al.*, *Mol. Cell* **11**, 853 (2003).
18. C. P. Lusk, T. Makhnevych, M. Marelli, J. D. Aitchison, R. W. Wozniak, *J. Cell Biol.* **159**, 267 (2002).
19. M. Marelli, J. D. Aitchison, R. W. Wozniak, *J. Cell Biol.* **143**, 1813 (1998).
20. U. Zabel *et al.*, *J. Cell Biol.* **133**, 1141 (1996).
21. D. Devos *et al.*, *Proc. Natl. Acad. Sci. U.S.A.* **103**, 2172 (2006).
22. D. Devos *et al.*, *PLoS Biol.* **2**, e380 (2004).
23. F. Alber *et al.*, *Nature* **450**, 695 (2007).
24. I. Chaudhuri, J. Soding, A. N. Lupas, *Proteins* **71**, 795 (2008).
25. J. Garcia De La Torre, M. L. Huertas, B. Carrasco, *Biophys. J.* **78**, 719 (2000).
26. Single-letter abbreviations for the amino acid residues are as follows: A, Ala; C, Cys; D, Asp; E, Glu; F, Phe; G, Gly; H, His; I, Ile; K, Lys; L, Leu; M, Met; N, Asn; P, Pro; Q, Gln; R, Arg; S, Ser; T, Thr; V, Val; W, Trp; and Y, Tyr.
27. V. Doye, R. Wepf, E. C. Hurt, *EMBO J.* **13**, 6062 (1994).
28. S. Siniossoglou *et al.*, *Cell* **84**, 265 (1996).
29. G. Drin *et al.*, *Nat. Struct. Mol. Biol.* **14**, 138 (2007).
30. P. Grandi, N. Schlaich, H. Tekotte, E. C. Hurt, *EMBO J.* **14**, 76 (1995).
31. S. Fath, J. D. Mancias, X. Bi, J. Goldberg, *Cell* **129**, 1325 (2007).
32. R. M. Bennett-Lovsey, A. D. Herbert, M. J. Sternberg, L. A. Kelley, *Proteins* **70**, 611 (2008).
33. N. Schrader *et al.*, *Mol. Cell* **29**, 46 (2008).
34. E. Conti, C. W. Muller, M. Stewart, *Curr. Opin. Struct. Biol.* **16**, 237 (2006).
35. A. Fotin *et al.*, *Nature* **432**, 573 (2004).
36. D. J. Owen, B. M. Collins, P. R. Evans, *Annu. Rev. Cell Dev. Biol.* **20**, 153 (2004).
37. S. M. Stagg *et al.*, *Cell* **134**, 474 (2008).
38. Y. Cheng, W. Boll, T. Kirchhausen, S. C. Harrison, T. Walz, *J. Mol. Biol.* **365**, 892 (2007).
39. J. E. Hinshaw, R. A. Milligan, *J. Struct. Biol.* **141**, 259 (2003).
40. B. Dujon, *Trends Genet.* **22**, 375 (2006).

41. We thank staff at beamlines 24-ID-C/-E at Argonne National Laboratory and X6A at National Synchrotron Light Source for excellent assistance with data collection, R. Sauer and T. Baker for critically reading the manuscript, G. Wink for contributions, members of the Schwartz laboratory for discussions, and the Biophysical Instrumentation Facility for the Study of Complex Macromolecular Systems (NSF-0070319 and NIH GM68762) for providing instrumentation. Supported by NIH grant GM77537 (T.U.S.), a Pew Scholar Award (T.U.S.), a Koch Fellowship Award (S.G.B.), and a Vertex Scholarship (S.G.B.). Coordinates and structure factors of the Nup85•Seh1 crystal structure have been deposited in the Protein Data Bank (PDB) with accession code 3EWE.

Supporting Online Material

www.sciencemag.org/cgi/content/full/1165886/DC1
Materials and Methods
Figs. S1 to S13
Tables S1 and S2
References

15 September 2008; accepted 16 October 2008
Published online 30 October 2008;
10.1126/science.1165886
Include this information when citing this paper.

Correction: 2 December 2008

www.sciencemag.org/cgi/content/full/1165886/DC1

Supporting Online Material for

Structural Evidence for Common Ancestry of the Nuclear Pore Complex and Vesicle Coats

Stephen G. Brohawn, Nina C. Leksa, Eric D. Spear, Kanagalaghatta R. Rajashankar, Thomas U. Schwartz*

*To whom correspondence should be addressed. E-mail: tus@mit.edu

Published 30 October 2008 on *Science* Express
DOI: 10.1126/science.1165886

This PDF file includes:

Correction (2 December 2008): This revision corrected several typographical errors have been corrected and improved the resolution of some of the figures.

Correction: 28 November 2008

Supporting Online Material

Protein Production and Purification

Full-length Seh1 and a proteolytically-mapped Nup85 fragment (residues 1-564) from *S.cerevisiae* were cloned into the bi-cistronic pCOLADuet bacterial expression plasmid (EMD Biosciences) using the BamHI/NotI and NdeI/XhoI restriction sites, respectively, resulting in N-terminally His-tagged Seh1 and untagged Nup85> The resulting plasmid was transformed into *E. coli* BL21(DE3)-RIL for protein expression. $Nup85_{1-564}$•Seh1 is referred to as Nup85•Seh1 in the paper for simplicity. Cells were grown at 30°C in Luria-Bertani broth supplemented with 0.4% glucose to OD_{600}= 0.8 and induced with 0.2 mM IPTG at 18°C for 18 hours. Cells were harvested by centrifugation, resuspended in 40 mM potassium phosphate pH 8.0, 500 mM NaCl, 20 mM imidazole, and 3 mM β-mercaptoethanol, and lysed using a french press. The crude lysate was centrifuged at 15,000g for 15 minutes. The soluble fraction was then incubated with 1 ml Ni-NTA per 1000 ODs for 30 minutes at 4°C and loaded onto a disposable column (Pierce). The column was washed with four bed volumes of 50 mM potassium phosphate pH 8.0, 400 mM NaCl, 30 mM imidazole, and 3 mM β-mercaptoethanol and the Nup85•Seh1 complex eluted in 4 bed volumes of 50 mM potassium phosphate pH 8.0, 250 mM NaCl, 250 mM imidazole, and 3 mM β-mercaptoethanol. Eluted protein was dialyzed against 10 mM Tris/HCl pH 8.0, 150 mM NaCl, 0.1 mM EDTA, and 1 mM DTT and the 6xHis-tag cleaved with PreScission protease. The protein was purified by anion exchange chromatography on a HiTrapQ column (GE Healthcare) via a linear NaCl gradient and twice by size exclusion chromatography using a Superdex S200 26/60 column (GE Healthcare) run in 10 mM Tris/HCl pH 8.0, 150 mM NaCl, 0.1 mM EDTA, and 1 mM DTT.

Selenomethionine derivatized Nup85•Seh1 was prepared by growing cells in M9 Medium (Sigma) supplemented with 1 mM $MgSO_4$, 6.6 μM $CaCl_2$, 1 ml $FeSO_4$ 4.2 mg/ml, 0.4% glucose, and 100 μl 0.5% (w/v) thiamine at 37°C (modified from (1)). At OD_{600}= 0.5 solid amino acid supplements were added (100 mg/ml L-lysine, L-phenylalanine, and L-threonine; 50 mg/ml L-isoleucine, L-leucine, L-valine, and L-selenomethionine). After 30 minutes, cultures were transferred to 22°C for 20 minutes and then induced with 0.2 mM IPTG for 18 hours. The selenomethionine-derivatized Nup85•Seh1 complex was purified as described for the native version. Incorporation of selenomethionine was confirmed by mass spectrometry (data not shown). Both the native protein and selenomethionine derivative were concentrated to 30 mg/ml for crystallization.

Full length Nup85 in complex with Seh1 ($Nup85_{1-744}$•Seh1, referred to as Nup85(fl)•Seh1) was cloned and purified like $Nup85_{1-564}$•Seh1.

Full-length Sec13 and $Nup145C_{109-712}$ from *S.cerevisiae* were cloned into the bi-cistronic pET-Duet bacterial expression plasmid using the BamHI/NotI and NdeI/XhoI restriction sites, respectively, resulting in N-terminally His-tagged Sec13 and untagged Nup145C. In order to stabilize the complex, the C-terminus of Sec13 and N-terminus of Nup145C were linked with a short flexible linker to generate a single chain. This linked version behaved identically to the complex made from separate chains with the advantage of increased stability and is here referred to as Nup145C•Sec13 for simplicity. The C-terminal tail module of Nup145C was removed from the construct to generate $Nup145C_{109-555}$•Sec13 by PCR and is referred to as Nup145CΔtail in the text. Nup145C-ELIEA•Sec13 and Nup145C(Q691G)•Sec13 were generated by PCR mutagenesis. Nup145C•Sec13 was produced identically to Nup85•Seh1 except that gel filtration was performed in 10 mM Hepes/NaOH pH 7.4, 150 mM NaCl, 1 mM DTT, 0.1 mM EDTA.

Correction: 28 November 2008

Full-length Nup84 from *S.cerevisiae* was cloned into a pET-Duet-derived plasmid using the BamHI/NotI restriction sites. The C-terminal tail module of Nup84 was removed from the construct to generate $Nup84_{1-482}$ by PCR and is referred to as Nup84Δtail in the text. Nup84-DSICD was generated by PCR mutagenesis. The protein was purified via metal-affinity and size exclusion chromatography as described for Nup145C•Sec13.
Full-length Nup120 from *S.cerevisiae* was cloned into a pET-Duet-derived plasmid using the BamHI/NotI restriction sites. A trimeric complex between full length Nup120, Nup85(fl), and Seh1 was produced essentially as in (18) and purified as described for Nup145C•Sec13.

Crystallization

The Nup85•Seh1 complex was crystallized in 18 % (v/v) PEG 3350, 0.2 M sodium citrate, and 0.1 M bis-tris-propane pH 8.5 by the hanging drop vapor diffusion method at 18°C. Crystals grew within 4-10 days forming rods with dimensions of 150 µm x 150 µm x 400 µm. The selenomethionine derivative crystallized in the same conditions. Native crystals were cryoprotected in reservoir solution with 15% (v/v) PEG 400. Se-Met crystals were cryoprotected in the reservoir solution supplemented with 4% (w/v) additional PEG 3350 before flash freezing in liquid nitrogen. Both the native and selenomethionine Nup85•Seh1 complex crystallized in space group $P4_12_12$ with two NCS-related heterodimers per asymmetric unit. Crystal screening was performed at beamline X6A at National Synchrotron Light Source (NSLS) and final X-ray data was collected at the NE-CAT beamline 24ID-C at Argonne National Laboratory.

Structure Determination

Data reduction was carried out using HKL2000 (2). The structure was solved with the single anomalous dispersion (SAD) technique using the SeMet derivative. The positions of 2*16 selenium sites (out of 2*20 possible) were found with the program SHELXD (3, 4) and were used for phasing. The NCS-averaged, solvent-flattened 3.7 Å experimental electron density map was of sufficient quality to trace the backbone of most of the model. The selenium positions served as markers to unambiguously assign the sequence for Nup85. Assigning the sequence of Seh1 was assisted by superimposing the structure of the homologous Sec13. The final model was refined against native data extending to 3.5 Å. Model building was carried out with Coot (5), for refinement the PHENIX suite was used (4). Only few packing interactions exist in the crystal, resulting in a relatively high Wilson B-factor of 118 $Å^2$. Thus, B-sharpened maps were generated with CNS (6, 7) and were used to assist side chain placement in the early stages of model building. NCS-restraints were applied throughout the refinement process. The final model has good stereochemistr (84.1% of residues in preferred regions, 14.4% in additional allowed regions) according to Molprobity (8). All secondary structure elements of the 100 kD heterodimer have been traced, however several loops connecting either helices in trunk and crown of Nup85 or strands in Seh1 are omitted due to poor electron density in those regions.

Analytical Gel Filtration

For Nup145C•Sec13 and Nup84 binding experiments, equimolar amounts of Nup145C•Sec13 (or Nup145C-ELIEA•Sec13) and Nup84 were mixed and incubated at 4°C for 5 minutes. Similarly, equimolar amounts of Nup145CΔtail•Sec13 and Nup84Δtail (or Nup84Δtail-DSICD) were mixed and incubated at 4°C for 5 minutes. Reactions (500 µl) were injected onto a Superdex S200 10/300 column (GE Healthcare) and run in 10 mM Hepes/NaOH pH 7.4, 150 mM NaCl, 1mM DTT, 0.1 mM EDTA at a flow rate of 0.8 ml/min.

Nup85•Seh1 complex at various concentrations (1, 5, 10, and 20 mg/ml) was loaded onto a Superdex S200 10/300 column and run in 10 mM Tris/HCl pH 8.0, 150 mM NaCl, 0.05 mM EDTA, and 0.5 mM TCEP at a flow rate of 0.8 ml/min.
In Supplemental Figure 5A, equimolar amounts of Nup145C•Sec13 and Nup85(fl)•Seh1 were mixed and incubated at 4°C for 5 minutes before injection on a Superdex200 HR26/60 column. In Supplemental Figure 5B, equimolar amounts of Nup120 and Nup85•Seh1 were mixed and incubated at 4°C for 5 minutes before injection on a Superose 6 HR10/300 column (GE Healthcare). In Supplemental Figure 6C, Nup120•Nup85(fl)•Seh1 was mixed with a 2-fold molar excess of Nup145C•Sec13 or Nup145CΔtail•Sec13 and incubated at 4°C for 5 minutes before injection on a Superdex S200 HR10/300 column. In Supplemental Figure 6, Ni-NTA elutions of Nup120•Nup85(fl)•Seh1 co-expressed with Nup145C-ELIEA•Sec13 or Nup145C(Q691G)•Sec13 (where both Nup120 and the Nup145C•Sec13 variant are 6xHis-tagged) were run on a Superdex200 HR26/60 column. Gel filtration was carried out in 10 mM Hepes/NaOH pH 7.4, 150 mM NaCl, 1mM DTT, 0.1 mM EDTA at the columns recommended flow rates.

Analytical Ultracentrifugation

Purified Nup85•Seh1 complex was gel-filtered in 10mM Tris/HCl pH 8.0, 150mM NaCl, 0.5 mM TCEP, and 0.05 mM EDTA immediately prior to the experiments. Analytical ultracentrifugation experiments were carried out with an Optima XL-A centrifuge using An50Ti (6 hole, equilibrium runs) or An60Ti (4 hole, velocity runs) rotors.
Samples for sedimentation velocity (440 µl sample or 450 µl buffer) were loaded into Epon-charcoal filled 2 channel centerpieces, fit with sapphire windows, and spun at 42,000 rpm. Concentrations of 6.3, 3.2, and 0.63 µM Nup85•Seh1 were used. Sedimentation velocity data was analyzed globally to generate a c(s) distribution using the hybrid local continuous distribution and global discrete species model in SEDPHAT (9). The data was fit from 2 to 10 s^{-13} with Sedanal calculated vbar = 0.7319 cm^3/g, η = 1.0182 cP, and ρ = 1.00472 g/ cm^3.
Samples for sedimentation equilibrium (110 µL sample or 120 µl buffer) were loaded into Epon-charcoal filled 6 channel centerpieces, fit with quartz windows, and spun at 13,500, 17,500, and 22,800 rpm, respectively. Two replicates of 6 concentrations (7.6, 6.3, 5.0, 3.8, 2.5, and 1.3 µM) were analyzed. Approach to equilibrium was monitored with Winmatch. Absorbance data was collected at 280 nm at the smallest possible step size with 5 replicates per step. Sedimentation equilibrium data (36 datasets total) were fit globally with Ultrascan 9.0 (http://ultrascan.uthscsa.edu) with a single ideal species model.

Isothermal Titration Calorimetry

Purified Nup145C•Seh1, Nup145C-ELIEA•Seh1, Nup145CΔtail•Seh1, Nup84, Nup84Δtail, and Nup84Δtail-DSICD were gel-filtered into 10 mM Hepes/NaOH pH 7.4, 150 mM NaCl, 1 mM DTT, and 0.1 mM EDTA immediately prior to the experiment. Protein concentrations were determined spectrophotometrically at 280 nm. ITC was performed using a VP-ITC microcalorimeter (MicroCal, Northampton, MA). Titrations were performed at 25ºC by injecting 6 µl aliquots of Nup145C•Seh1, Nup145C-ELIEA•Seh1, or Nup145CΔtail•Seh1 at 4.8 µM into the ITC cell containing 1.43 ml of Nup84, Nup84Δtail, or Nup84Δtail-DSICD at 0.4 µM. Binding stoichiometry, enthalpy and entropy as well as the equilibrium dissociation constant was determined by using the "single set of independent sites" model of molecular association (MicroCal Origin 2.9; MicroCal).

Correction: 28 November 2008

CD Spectroscopy

Nup145CΔtail•Sec13, Nup145CΔtail-ELIEA•Sec13, Nup84Δtail, and Nup84Δtail-DSICD were purified as described above and gel filtered into 5 mM Hepes/NaOH pH 7.4 and 150 mM NaCl immediately prior to the experiment. An Aviv Model 202 CD spectrometer was used for all experiments. CD signal at 208nm of 1.3 μM protein in a 1 mm pathlength cell was recorded at every degree during a 25-80˚C temperature ramp with two minutes of equilibration time at each step.

***In Vivo* Localization Experiments**

Strains were grown in YPD (1% yeast extract, 2% yeast peptone, 2% glucose) at 24°C to an OD_{600} of 0.5-0.8. Cells were added to an equal volume of phosphate buffered saline (PBS, pH 7.3) with 20 mg/ml Hoechst dye (Invitrogen) for 30 min at room temperature to stain DNA. Cells were harvested by centrifugation, washed once in phosphate buffered saline (PBS) and viewed using a Nikon E800 fluorescent microscope (Melville, NY) mounted with a Hamamatsu digital camera (Bridgewater, NJ). Images were captured using Improvision OpenLabs 2.0 software (Lexington, MA) with identical exposure times for each sample. Final images were constructed using Adobe Photoshop CS3 and Adobe Illustrator CS3 (Adobe Systems).

Yeast Plasmid Construction

The CEN/ARS plasmid SBYp115 containing the entire *NUP145* gene with the *NUP145* promoter and 3' UTR was constructed by gap repair in yeast. Sequences upstream and downstream of the *NUP145* ORF (–800 to –100 and +1 to +400) were amplified by PCR using Phusion DNA polymerase (New England BioLabs) with primer combinations oES143 (5'- aaaggatccGCAACACTTTCAATTGCATTTCTTCAA-3') with oES144 (5'- tttgaattcCAAACGAGTTAATTCTTTCTAATTTTT-3') and oES145 (5'- tatgaattcGACTGAAGCTAACGCTTTTGGAGTAAT-3') with oES146 (5'- aaagtcgacGAAAGAGATAGATTTCTGTAAGAAGGC-3'), respectively. The PCR products were cloned into the *Bam*HI/*Sal*I sites of pRS316 to make pES323. Gap repair of *Eco*RI-digested pES323 resulted in full-length *NUP145* in pRS316 (SBYp115). Plasmid SBYp116 (*NUP145, LEU2, CEN*) was constructed by ligating a *Bam*HI-*Sal*I fragment from SBYp115 into pRS315 (10). Plasmid SBYp117 (*nup145C-ELIEA, LEU2, CEN*) was constructed by ligating a 1.5 kb *Aat*II-*Avr*II fragment from pSB210 into the same site of SBYp116.

Strain Construction

Yeast strains used in this study are listed in Table S2. Genomic tagging of *NUP133* and *NUP84* in a *NUP145/nup145::KANMX4* diploid (BY4743 background, *Saccharomyces cerevisiae* deletion consortium) was done by homologous recombination (11) using pYM28 (*eGFP:HIS3MX6*) as template. Strains were selected on SMM-histidine plates and verified by western blotting with anti-GFP antibody and nuclear rim localization of the Nup-GFP chimeric proteins. The resulting diploids were transformed with SBYp115 (*NUP145, URA3, CEN*) to allow viable colonies following sporulation and tetrad dissection. Haploid strains were then transformed with SBYp116 (*NUP145, LEU2, CEN*) or SBYp117 (*nup145C-ELIEA, LEU2, CEN*), grown in medium lacking leucine, and plated on 5-fluoroorotic acid plates (fig. S8).

Cell fractionation

Strains expressing Nup133-GFP or Nup84-GFP were grown to log phase (OD_{600} = 0.5-0.7) in YPD at 30°C. 25 OD_{600} units were harvested by filtration, washed with cold

water, and collected by centrifugation. Cells were pre-treated with 100mM Tris/HCl, pH 9.4, 0.5% 2-mercaptoethanol for 10 min at 30°C and spheroplasted in S buffer (40 mM Hepes/NaOH pH 7.5, 5 mM $MgCl_2$, 1.2 M sorbitol) containing 0.2mg/ml Zymolyase (100T) for 1 hour at 30°C. Spheroplasts were washed 3 times with S buffer, resuspended in 0.5 ml lysis buffer containing 20 mM HEPES, pH 7.5, 5 mM $MgCl_2$, 1 mM PMSF and protease inhibitor cocktail (Roche) and lysed on ice by Dounce homogenization. A portion of the total lysate was removed (T), and the remaining lysate was centrifuged at 16,000g for 30 min at 4°C resulting in a soluble (S) and pellet (P) fraction. Equal cell equivalents were resolved by SDS-PAGE, transferred to nitrocellulose, and proteins were detected using antibody against GFP (1:20,000) or the cytosolic protein Pgk1p (1:3,000).

Correction: 28 November 2008

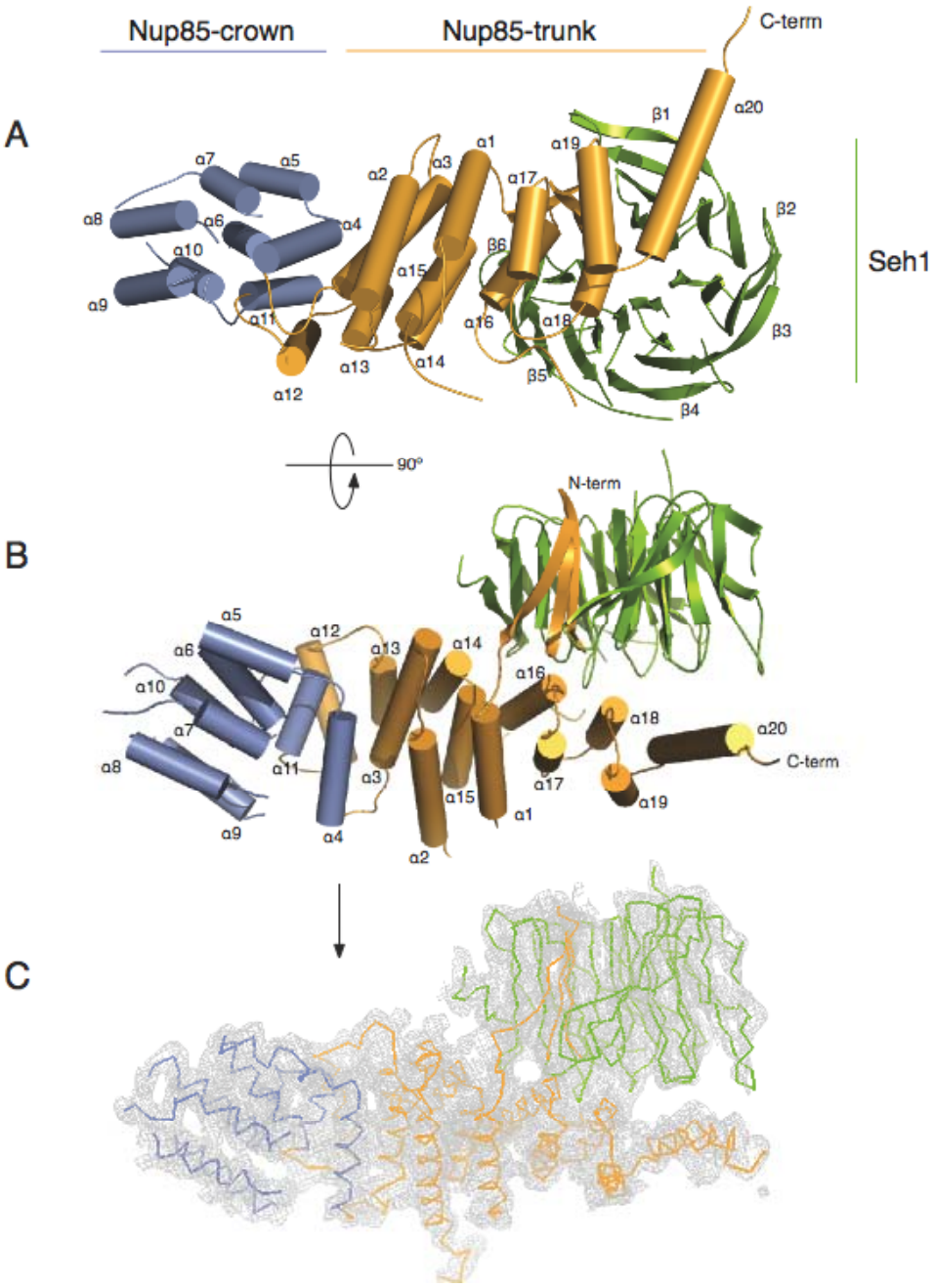

Fig. S1 – Structure of the Nup85•Seh1 complex.
The structure of the heterodimeric Nup85•Seh1 complex is shown in two views **(A, B)**, related by a 90° rotation around the horizontal axis. Nup85 has a trunk (orange, helices α1-α3 and α12-α20) and a crown (blue, helices α4-α11) module. The β-strands at the extreme N-terminus of Nup85 form an insertion blade, which complete the Seh1 (green) β-propeller. **(C)** $2F_o$-F_c omit map (contoured at 1.2σ) with a Cα-trace of the Nup85•Seh1 complex.

Correction: 28 November 2008

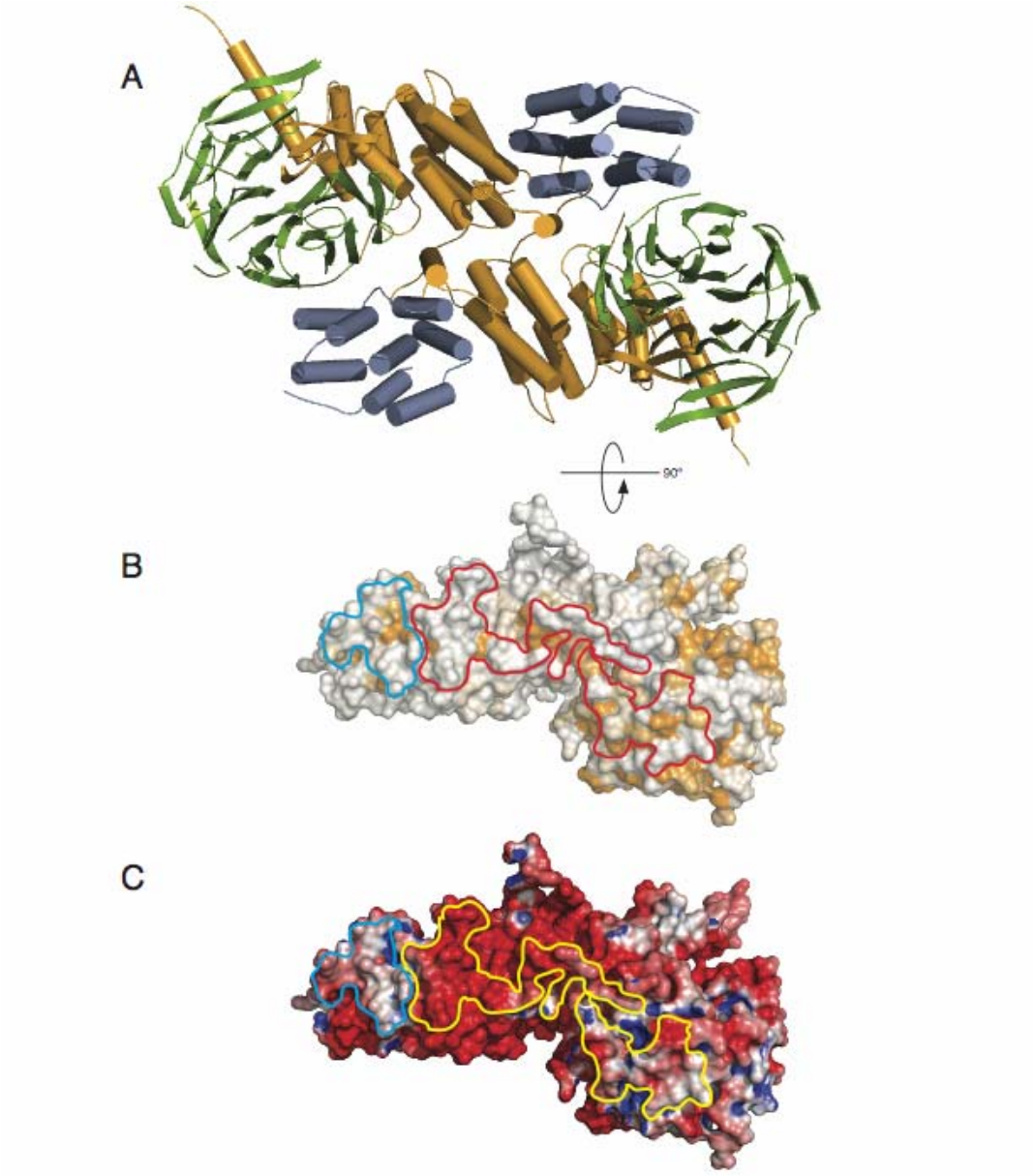

Fig. S2. Arrangement of two Nup85•Seh1 heterodimers in the asymmetric unit.

(A) Association and orientation of the two Nup85•Seh1 heterodimers in the asymmetric unit. The heterodimers form an interface of ~1300 Å^2 and associate lengthwise along a two-fold axis. **(B)** Surface conservation of Nup85•Seh1 in a view 90° rotated from the lower molecule in **(A)** with outlines corresponding to contact regions involved in forming the interface. Red and blue outlines indicate contacts made with Nup85 and Seh1, respectively, and conservation is shaded from white (not conserved) to orange (conserved). **(C)** The electrostatic surface potential of the Nup85•Seh1 heterodimer (colored from red (-8 kT/e) to blue (+8 kT/e)) with outlines as in **(B)**. Yellow and blue outlines correspond to contacts made with Nup85 and Seh1, respectively. The view is the same as in **(B).**

Correction: 28 November 2008

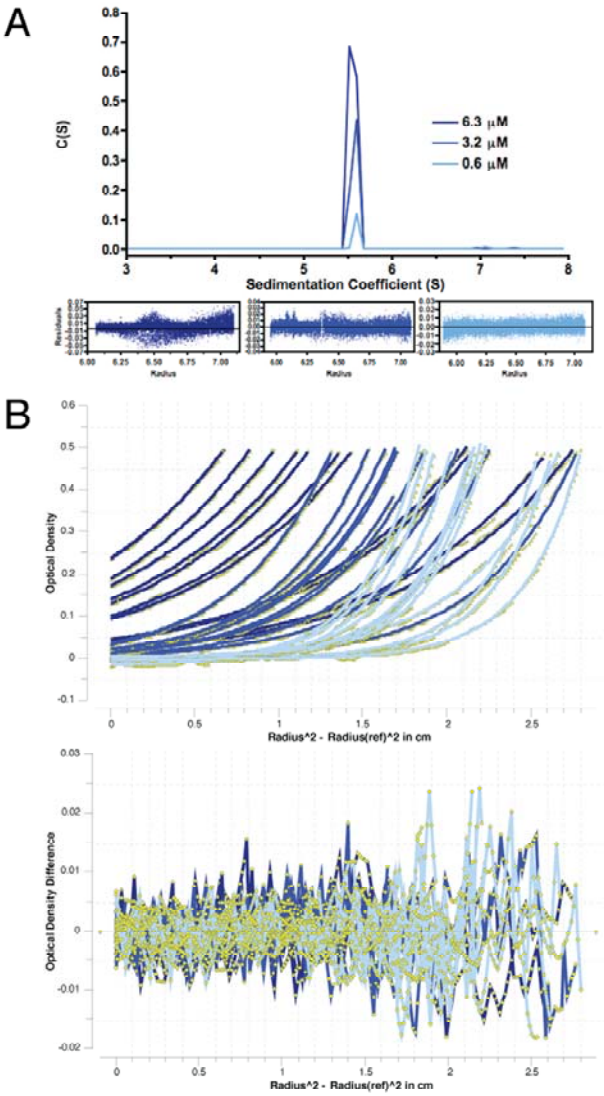

Fig. S3. Nup85•Seh1 is a heterodimer in solution as determined by analytical ultracentrifugation.

(A) C(s) distribution analysis of Nup85•Seh1 sedimentation velocity data. Sedimentation data from three concentrations of Nup85•Seh1 were analyzed globally in Sedphat (9) with a hybrid local continuous distribution and global discrete species model. Data was fitted from 2 to 10 s^{-13} with fixed partial specific volume. Residual plots for each concentration are shown below. The sedimentation coefficient and corresponding rmsd values for the samples in order of decreasing concentration were 5.56 s^{-13} , 5.58 s^{-13}, and 5.60 s^{-13} and 0.0079, 0.0056, and 0.0045, respectively, which corresponds to a single species with a molecular weight of ~104 kD and frictional ratio (f/f0) of 1.43. The calculated molecular weight for Nup85•Seh1 is 103 kD. **(B)** Sedimentation equilibrium analysis of Nup85•Seh1. Sedimentation data from 6 concentrations at three speeds were analyzed globally in Ultrascan 9.0. The data was best fit by an ideal single species model. The top panel shows data points as yellow triangles with fit curves overlaid (13.5 krpm – dark blue, 17.5 krpm – medium blue, 22.8 krpm – light blue). The lower panel shows residuals of the fitted curves. The molecular weight was determined to be 99 kD with a standard deviation of 0.4 kD, closely matching the results obtained via sedimentation velocity.

Correction: 28 November 2008

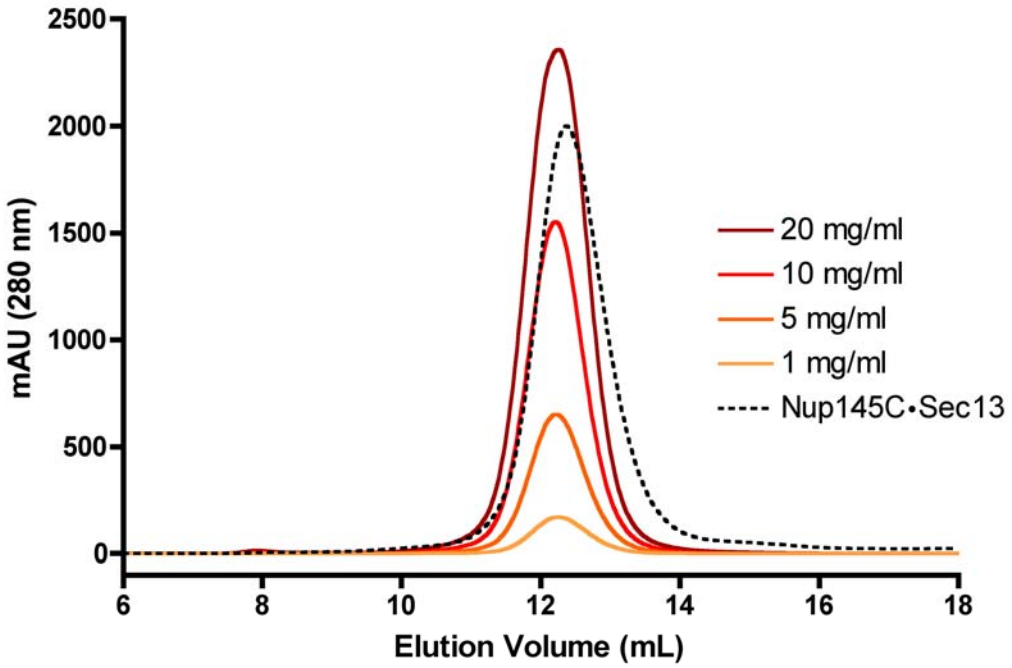

Fig. S4. Nup85•Seh1 is a heterodimer in solution as determined by size exclusion chromatography.

Elution profiles of the $Nup85_{1\text{-}564}$•Seh1 complex at 1, 5, 10, and 20 mg/ml show a single peak eluting at 12.2 ml on a Superdex 200 10/300 (GE Healthcare) column indicating a hydrodynamic radius of 4.4 nm. The hydrodynamic radius was independently determined by sedimentation velocity and is consistent with the value calculated from the experimental crystal structure using HYDROPRO (12). The elution profile of Nup145C•Sec13 is shown for comparison (dashed black line).

Correction: 28 November 2008

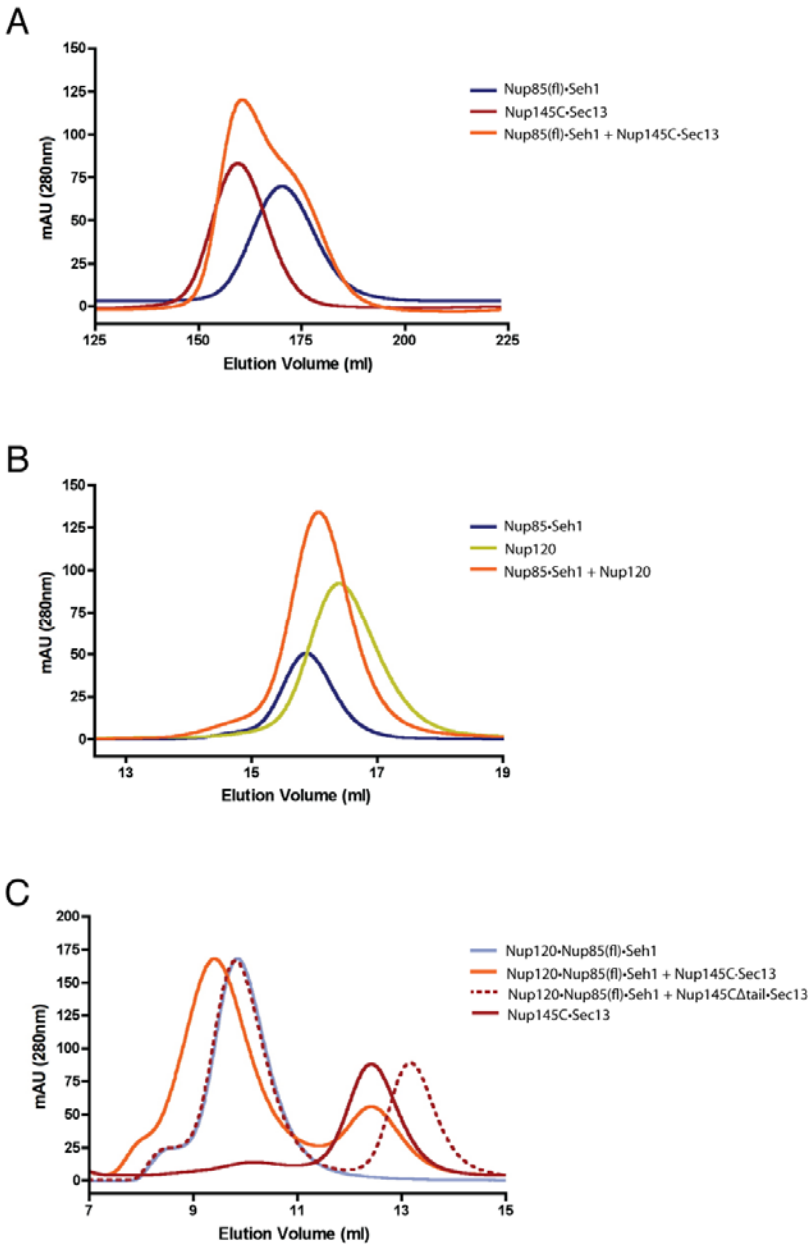

Fig. S5. Nup120 binds Nup145C and Nup85 via their tail modules.

(**A**) The heterodimeric Nup85(fl)•Seh1 and Nup145C•Sec13 complexes were analyzed on a Superdex200 HR26/60 column. A mixture of both complexes (orange) does not result in a higher molecular weight species indicating that the complexes do not directly interact. (**B**) The heterodimeric Nup85•Seh1 complex (without the Nup85 tail module) and Nup120 were analyzed on a Superose 6 HR10/300 column. Again, a mixture of both samples (orange) does not result in a higher molecular weight species. (**C**) Nup85(fl)•Seh1 including the tail module binds Nup120 (blue), and adding Nup145C•Sec13 results in a pentameric complex (orange) (Superdex S200 HR10/300). This complex is not formed when the tail module is removed from Nup145C (dashed). Taken together, this series of experiments demonstrates that the tail modules of both Nup145C and Nup85 are responsible for Nup120 binding.

Correction: 28 November 2008

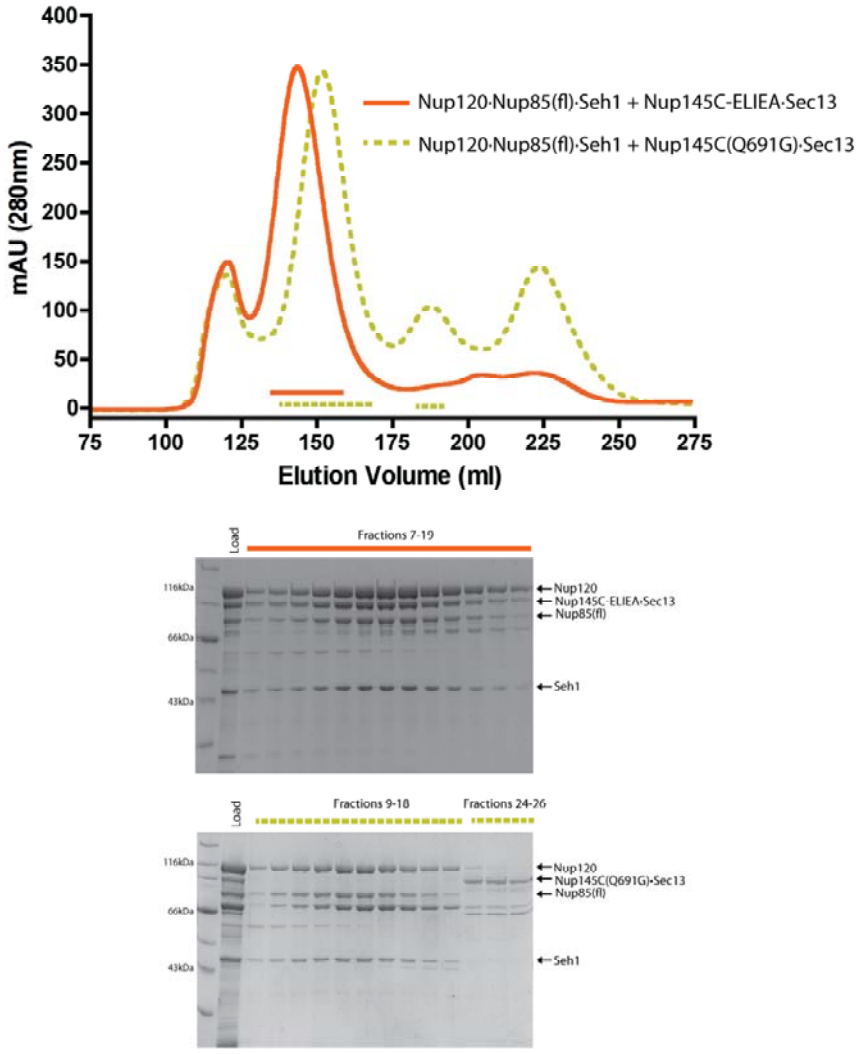

Fig. S6. A single point mutation in the predicted interaction helix of the Nup145C tail module disrupts Nup120 binding.

Formation of a pentameric Nup120•Nup85(fl)•Seh1•Nup145C-ELIEA•Sec13 complex (orange) is disrupted by the Q691G mutation in the tail module of Nup145C (dashed) (Superdex S200 HR26/60). Formation of the Nup120•Nup85•Seh1 complex is unaffected by this mutation. Fractions were analyzed by SDS-PAGE.

Correction: 28 November 2008

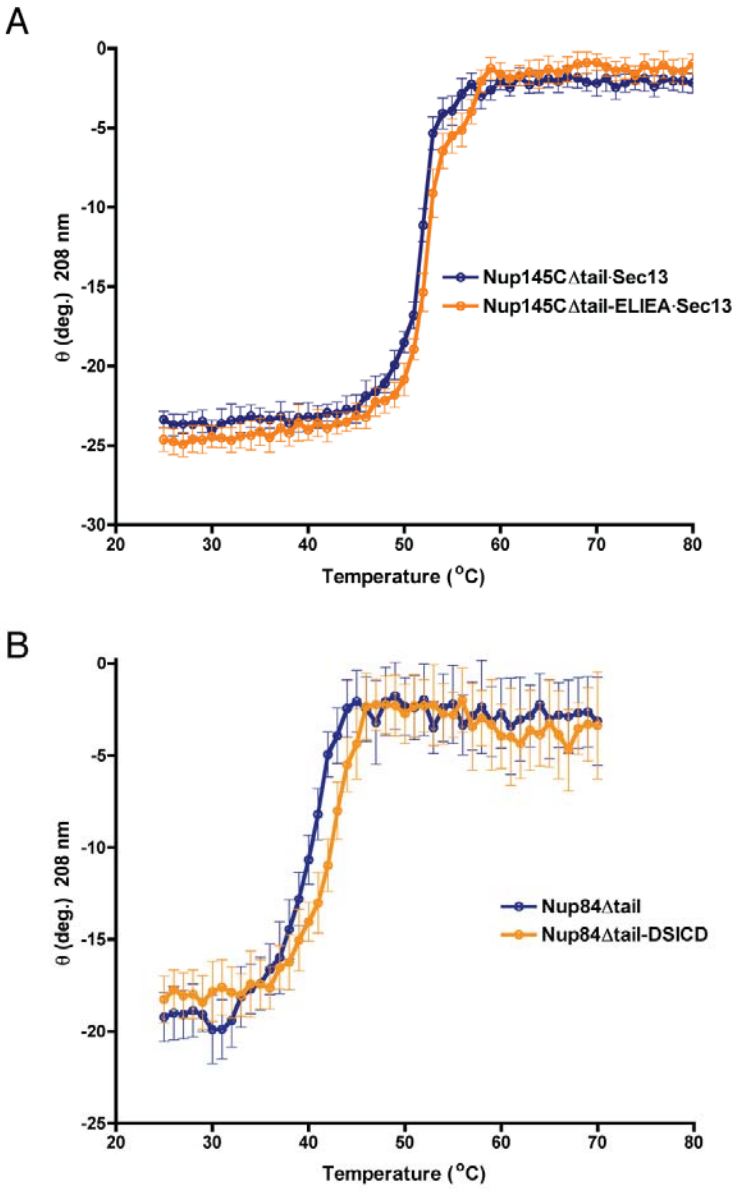

Fig. S7. Surface mutation of the Nup145C and Nup84 crowns does not negatively affect protein stability.

(**A**) Heat denaturation of Nup145CΔtail•Sec13 and Nup145CΔtail-ELIEA•Sec13 monitored by circular dichroism. Ellipticity at 208 nm is plotted as a function of temperature. The melting temperature, T_m, is nearly identical at ~52 °C for both protein complexes. (**B**) Nup84Δtail and Nup84Δtail-DISCD also have very similar thermal denaturation characteristics (T_m, ~41 °C) indicative of uncompromised protein stability.

Correction: 28 November 2008

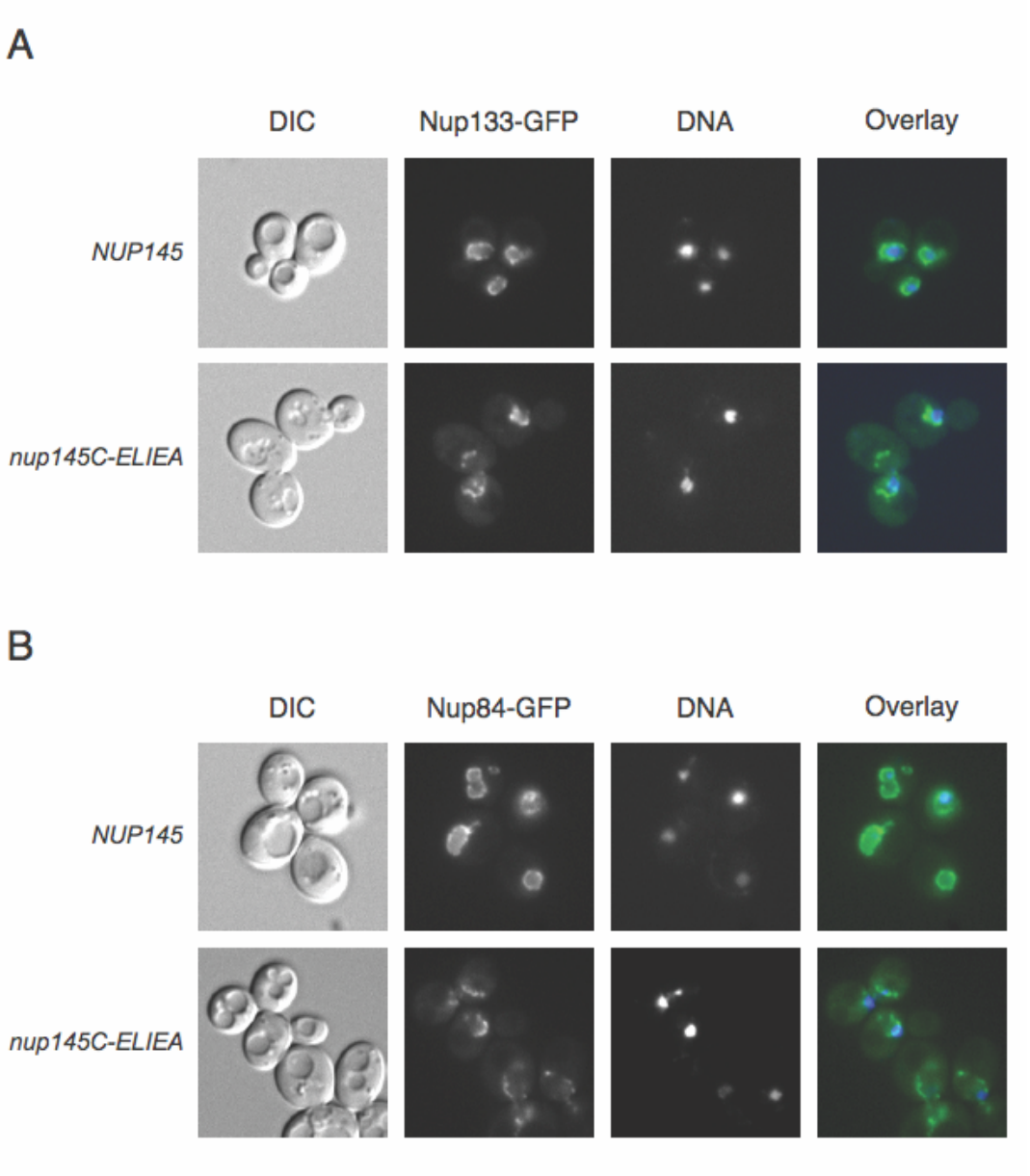

Fig. S8 – Elimination of the Nup84 binding site on Nup145C results in nuclear pore assembly defects *in vivo*.

(A) *NUP145/NUP133-GFP* and *NUP145-ELIEA/NUP133-GFP* or **(B)** *NUP145/NUP84-GFP* and *NUP145-ELIEA/NUP84-GFP* were grown at 24 °C and visualized by fluorescence microscopy. DIC, GFP-fluorescence, DNA (visualized with Hoechst dye), and false-colored overlay (GFP fluorescence – green, DNA – blue) images of the same field are shown in columns from left to right.

Correction: 28 November 2008

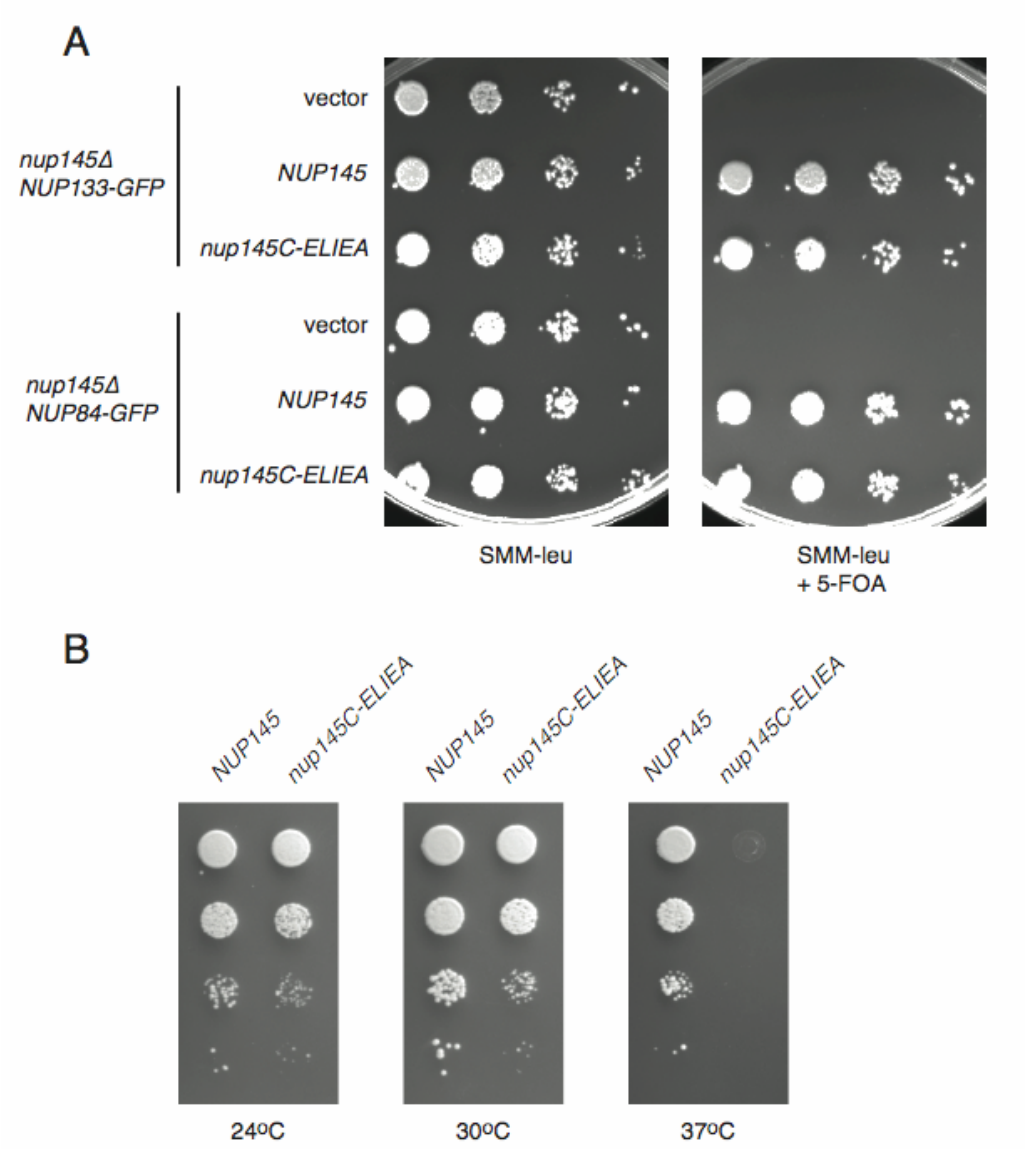

Fig. S9. Growth analysis of yeast strains.

(A) The nup145C-ELIEA mutant supports viability. *nup145Δ/NUP133-GFP* and a *nup145Δ/NUP84-GFP* strain carrying SBYp115 (*NUP145/CEN/URA3*) and empty vector, or vector encoding *NUP145*, or vector encoding *nup145C-ELIEA* were grown in SMM-leu overnight, serially diluted and grown on SMM-leu or SMM-leu + 5-FOA plates at 30°C for two days. **(B)** *nup145C-ELIEA* is lethal at elevated temperatures in rich media. A *nup145Δ* strain carrying plasmid-borne *NUP145* (SBYp116) or *nup145C-ELIEA* (SBYp117) were grown in minimal medium at 24°C. Serial-diluted cells were plated onto YPD plates and grown for 2 days at 24°C, 30°C or 37°C.

Correction: 28 November 2008

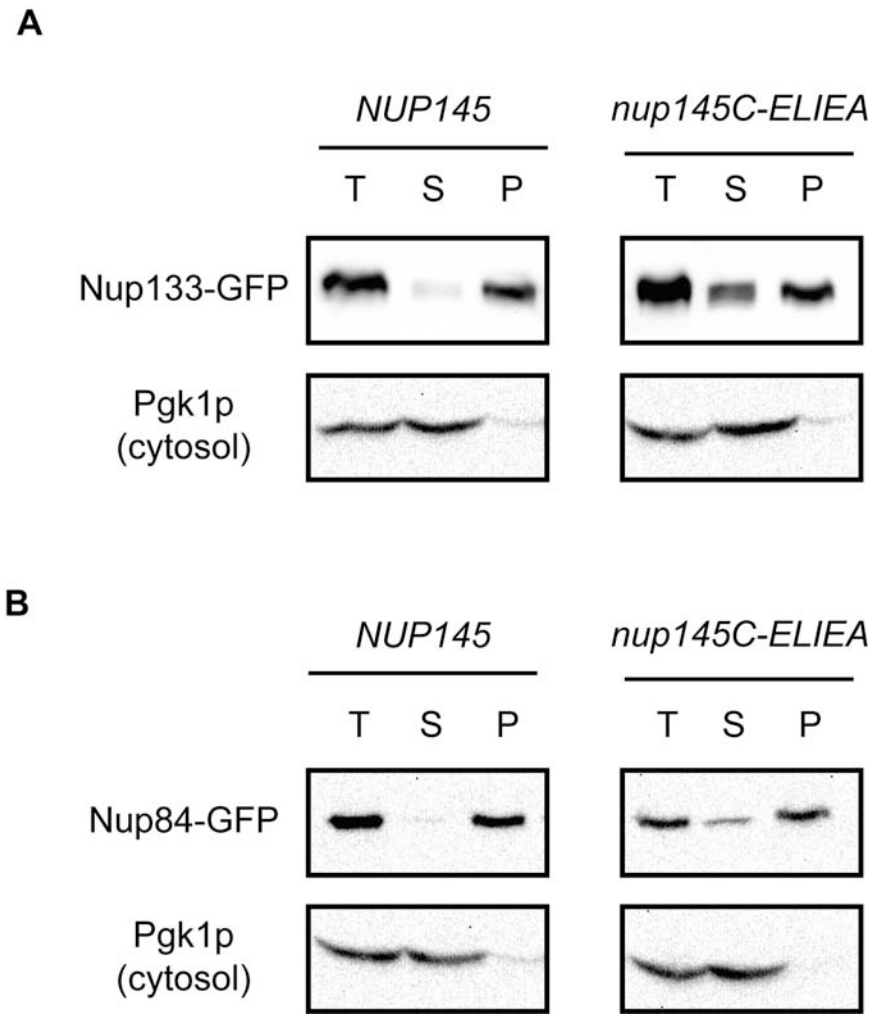

Fig. S10. Nup133-GFP and Nup84-GFP become more soluble in the Nup145-ELIEA strain.

(A) *NUP145 NUP133-GFP* (YS221) and *nup145C-ELIEA NUP133-GFP* (YS222) or **(B)** *NUP145 NUP84-GFP* (YS223) and *nup145C-ELIEA NUP84-GFP* (YS224) strains were spheroplasted, and total lysates (T) were separated into 16,000g soluble (S) and pellet (P) fractions. Equal cell equivalents from each fraction were analyzed by immunoblotting using rabbit anti-GFP or monoclonal anti-Pgk1 antibodies.

Correction: 28 November 2008

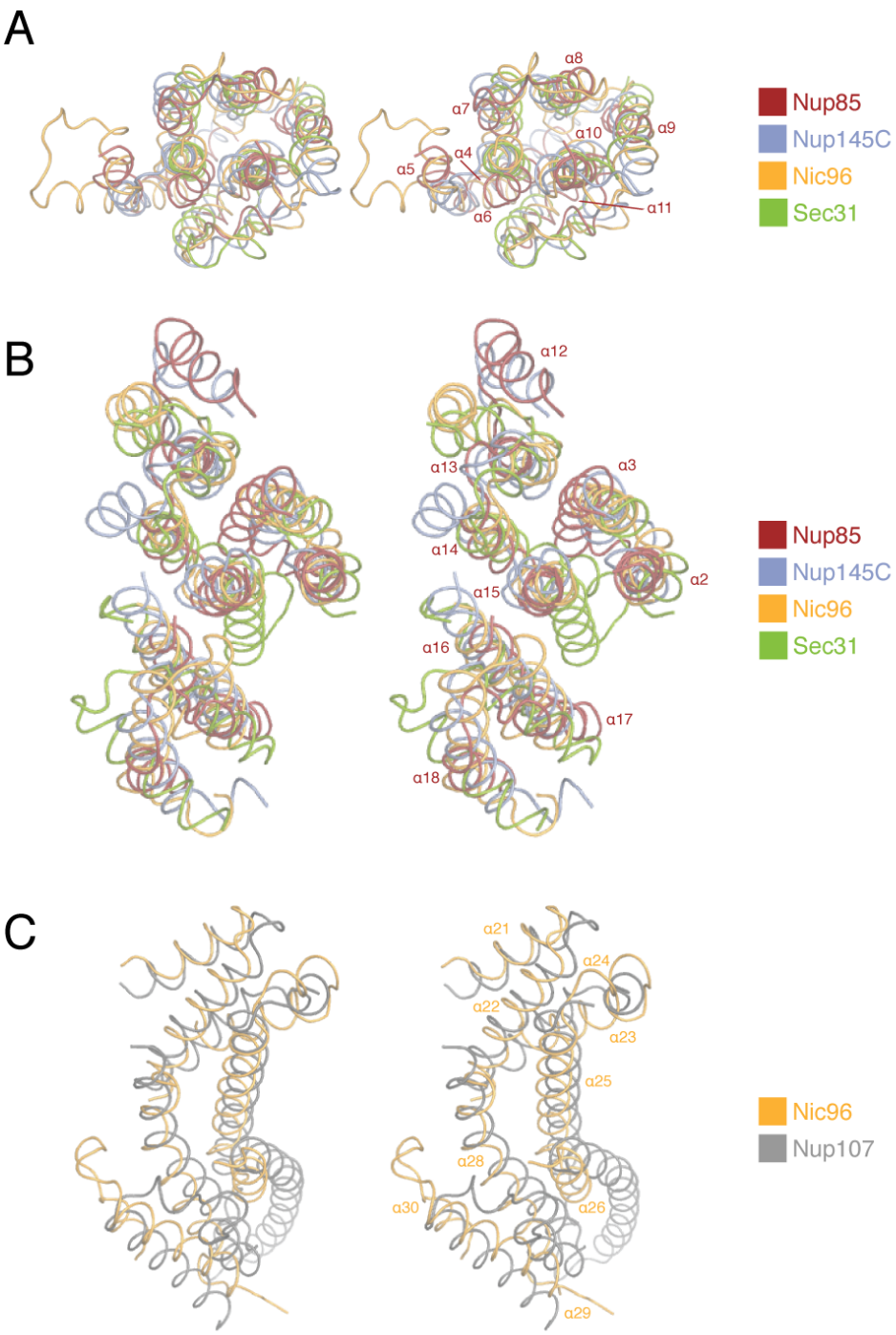

Fig. S11 – Superposition ACE1 modules.

Superposition of **(A)** crowns, **(B)** trunks, and **(C)** tails of ACE1 with known structures (PDB accession codes 3BG1, Nup145C; 2QX5, Nic96; 3CQC, Nup107; 2PM6, Sec31). Helices are labeled according to Nup85 in **(A)** and **(B)** and Nic96 in **(C)**. In **(A)** Helix α4 of Sec31 and the short beta sheet between helices α5 and α6 in Nic96 are omitted for clarity. The rmsd between modules is 2.9-3.2 Å in **(A)**, 3.4-3.5 Å in **(B)** and 2.7 Å in **(C)**.

Correction: 28 November 2008

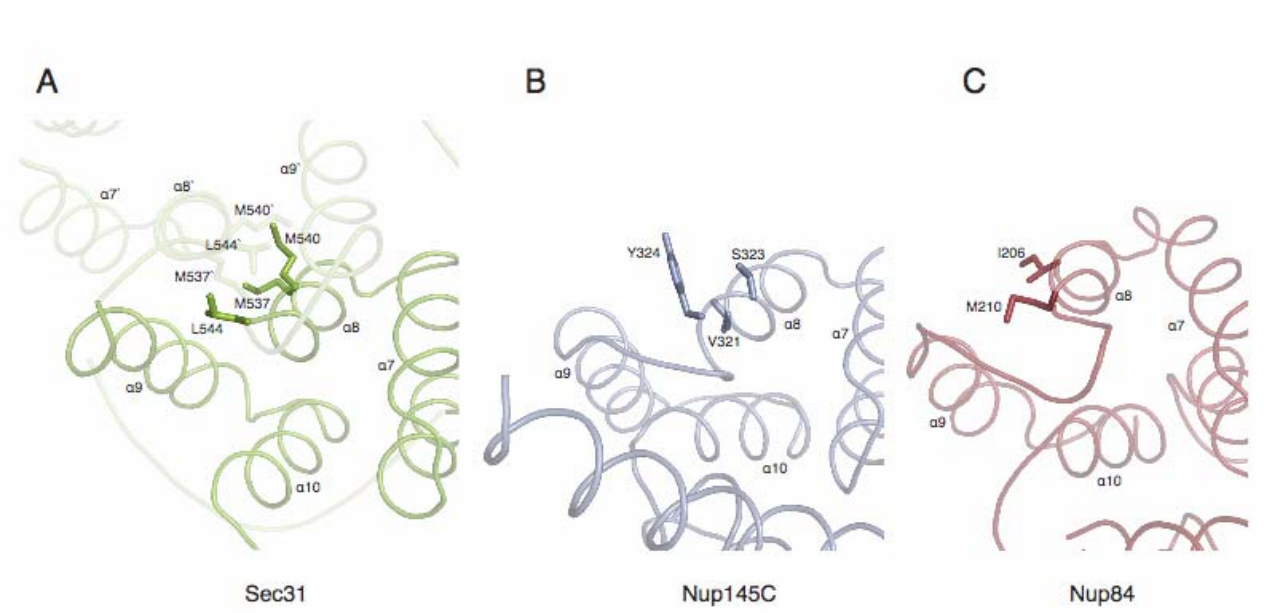

Fig. S12. Surface mutations of the Nup145C and Nup84 crowns.
The crown helix α8 is highlighted in **(A)** Sec31 (PDB code 2PM6) **(B)** Nup145C (PDB code 3BG1) and **(C)** Nup84. In **(A)**, one Sec31 monomer is shown half transparent and the three hydrophobic residues buried in the interaction between crown helix α8 in each monomer are shown as sticks. In **(B)**, the three exposed α8 residues in Nup145C mutated to disrupt binding to Nup84 are shown (VLISY to ELIEA**).** In **(C)**, the two exposed hydrophobic α8 residues in the Phyre-predicted Nup84 structure mutated to disrupt Nup145C binding are shown (ISICM to DSICD).

Correction: 28 November 2008

A Nup85

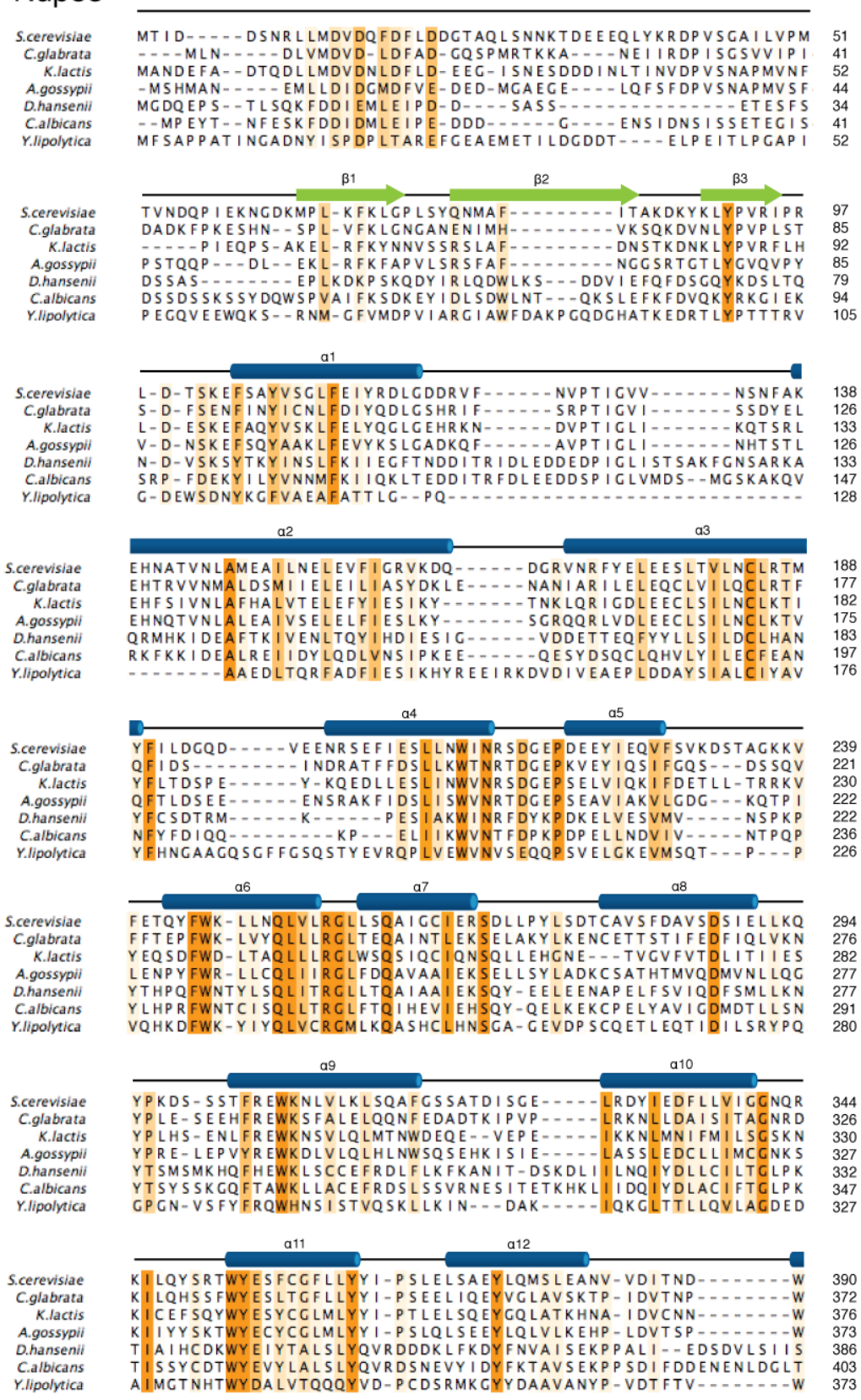

Correction: 28 November 2008

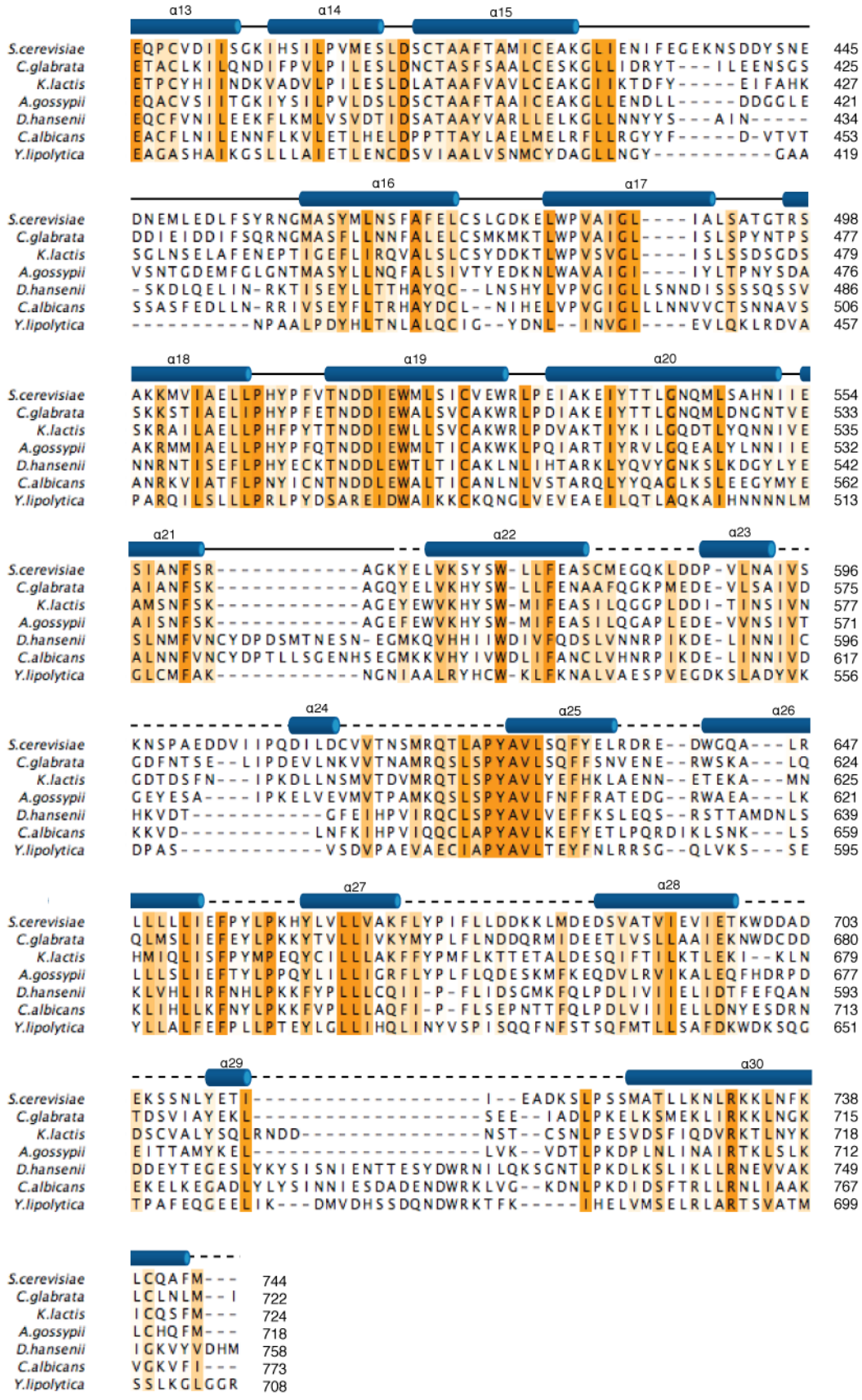

Correction: 28 November 2008

B Nup145C

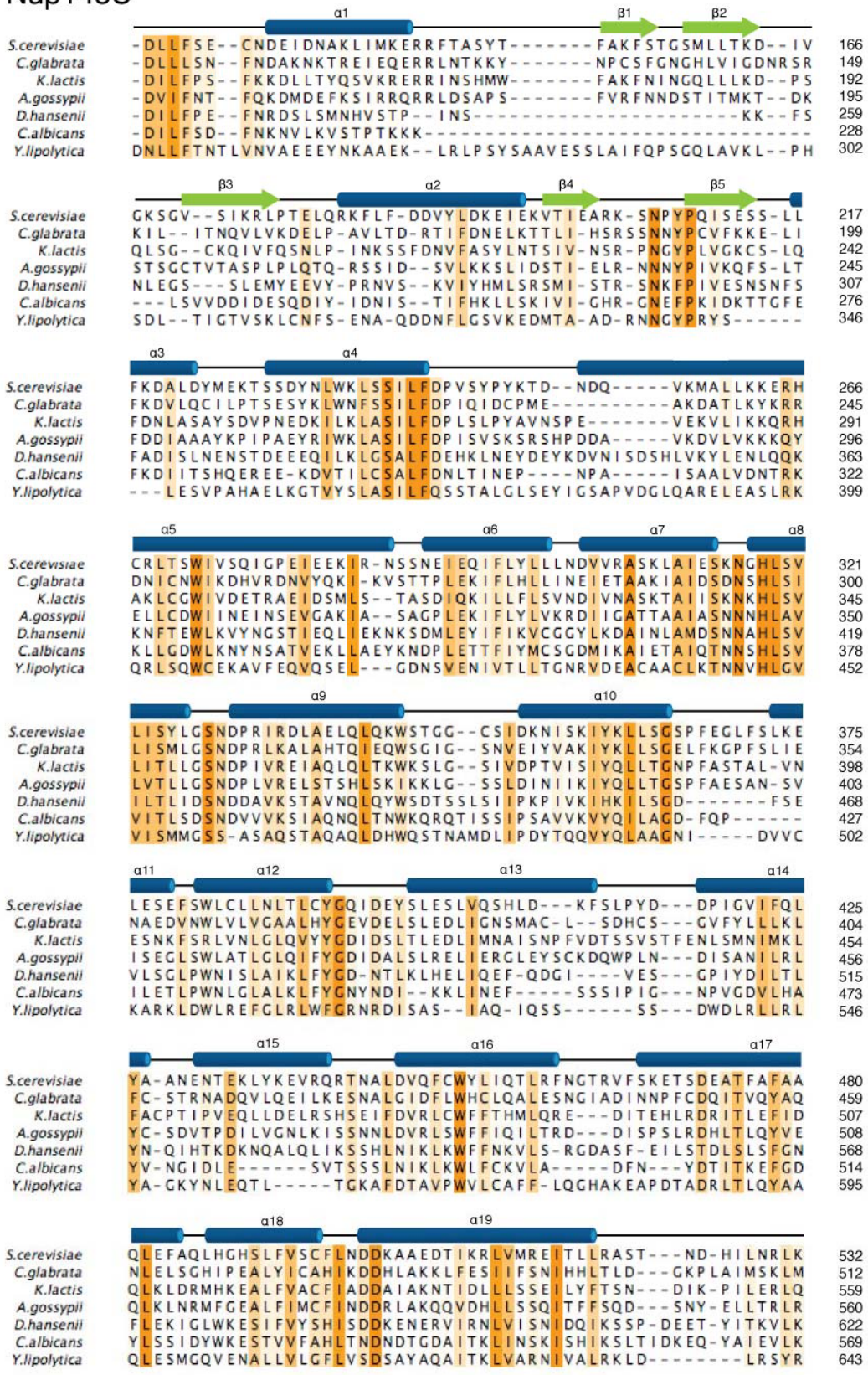

Correction: 28 November 2008

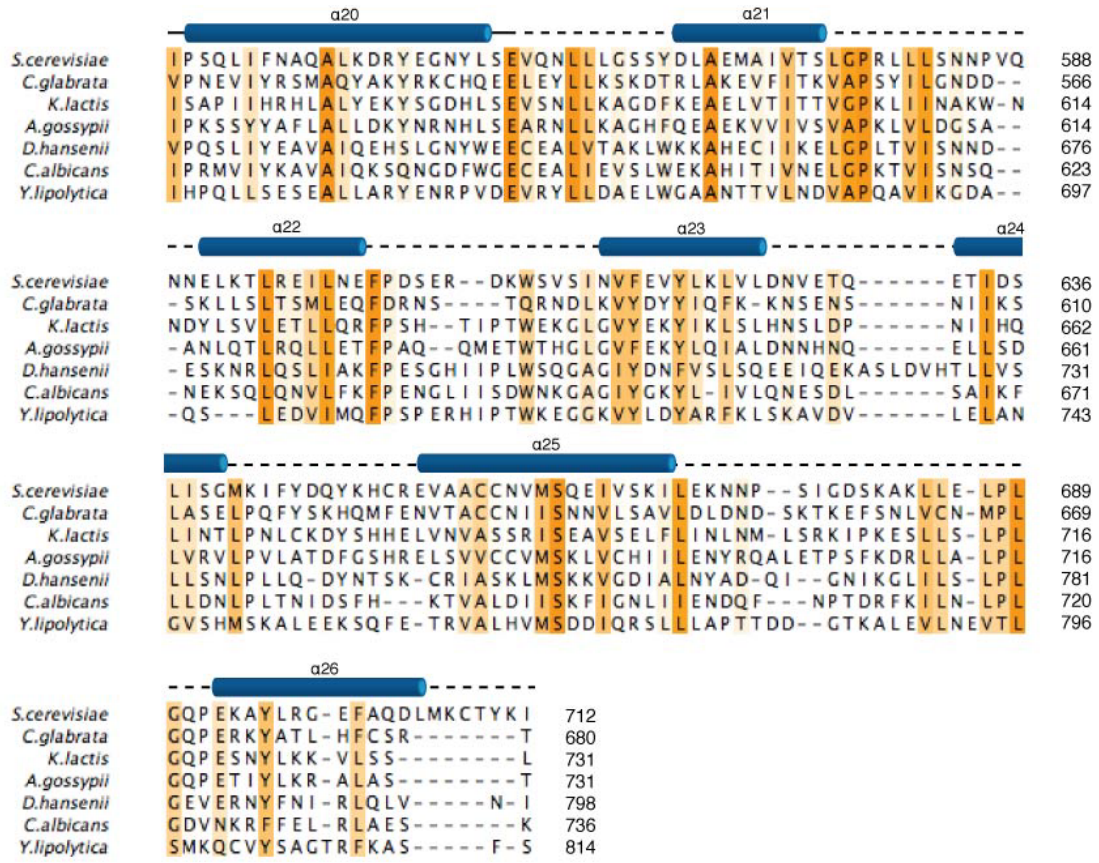

Correction: 28 November 2008

C

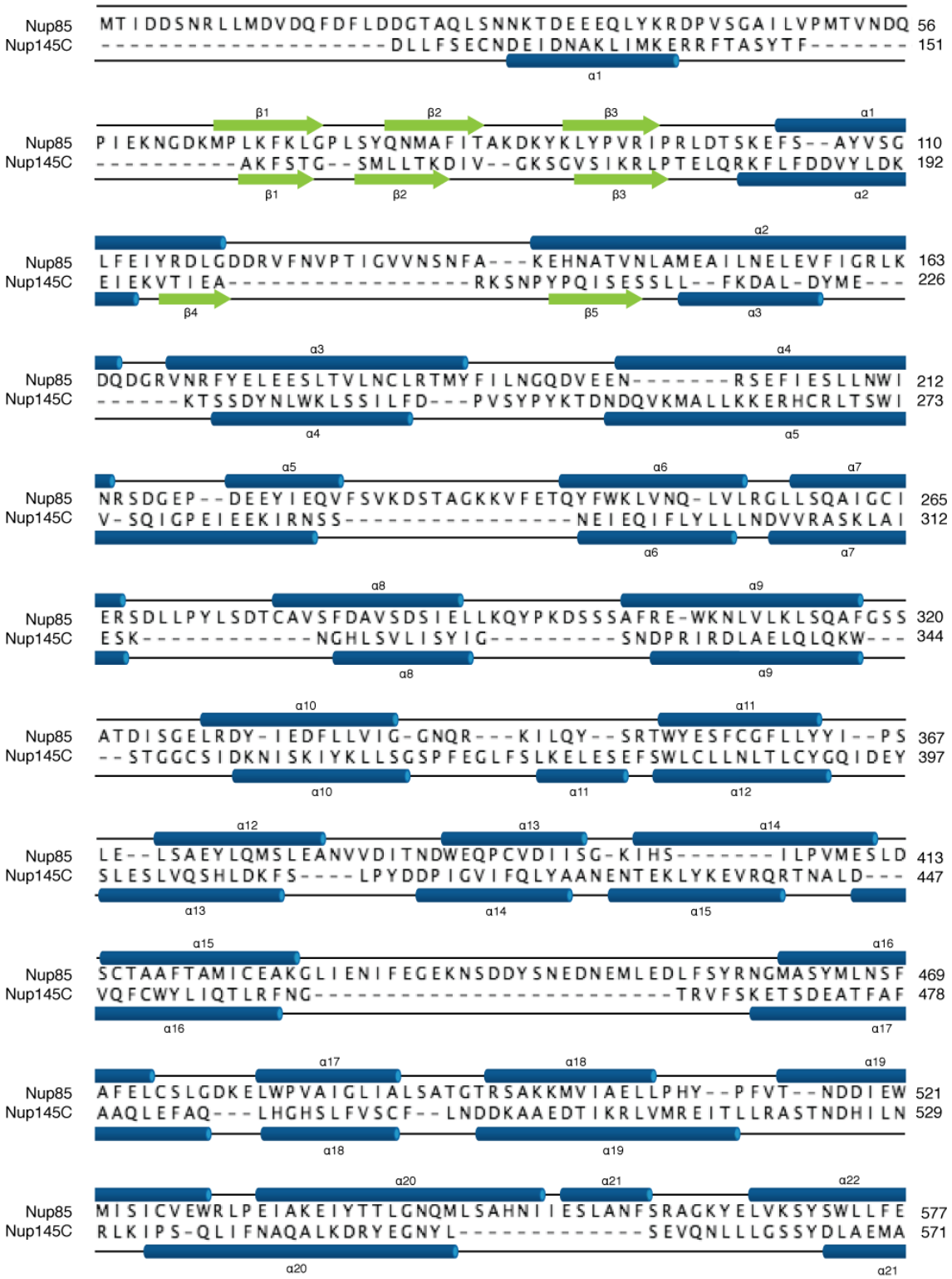

Correction: 28 November 2008

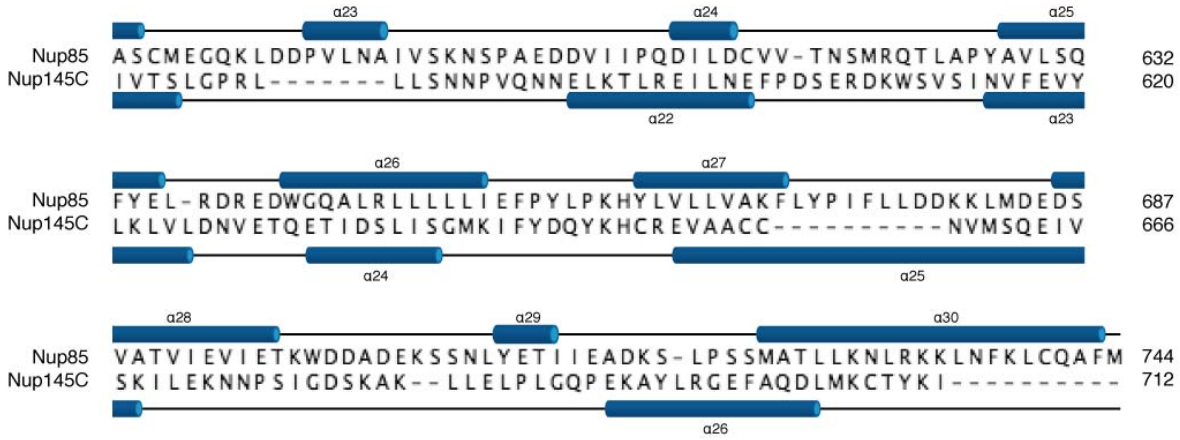

Fig. S13. **Sequence alignments.**

Multiple sequence alignments of **(A)** Nup85 and **(B)** Nup145C covering the phylogenetic spectrum of budding yeasts. The alignment for Nup145C begins after the N-terminal unstructured region at residue 123. Sequence alignments were performed with 3D-Coffee (13) (using the known structures) and illustrated with Jalview (14). Sequence conservation is colored from white (not conserved) to orange (highly conserved). The secondary structure is shown above the sequences and was assigned using information from the known structures and predictions from PredictProtein (15). Dashed lines denote the C-terminal regions absent from the known structures. **(C)** Pairwise alignment of Nup85 and Nup145C from *S. cerevisiae*. The alignment was made by combining DALI (16) results using the structures with an alignment from T-Coffee (17) corresponding to the tail modules. The secondary structure for Nup85 and Nup145C is shown above and below the sequences, respectively, and was assigned from the structures and predictions from PredictProtein.

Correction: 28 November 2008

Table S1 - Data collection and refinement statistics.

Data Set	$Nup85_{1-564}$•$Seh1_{1-349}$ Native	$Nup85_{1-564}$•$Seh1_{1-349}$ SeMet (Se Peak)
Data Collection		
Wavelength	0.9792	0.9792
Space group	$P4_12_12$	$P4_12_12$
Cell dimensions:		
a=b, c (Å)	112.6, 350.5	112.5, 351.2
Unique reflections	29579	45741
Resolution (Å)	40-3.4	50-3.7
R_{sym}[a]	10.7	12.7
Completeness	96.9 (98.8)	99.1 (99.9)
Redundancy	3.1 (3.3)	6.3 (6.1)
I/σ	13.7 (1.8)	21.9 (1.8)
Refinement		
Resolution (Å)	30-3.5	
Unique reflections	28300	
Protein / Non-protein atoms	9636 / 0	
R_{work}[b]	32.6	
R_{free}[c]	36.9	
RMSD Bond lengths (Å)	0.008	
RMSD Bond angles (°)	1.2	
Estimated coordinate error (Å)	0.58	

[a] $R_{sym} = \sum|I_i - \langle I_i \rangle| / \sum I_i$, where I_i is the intensity of the *i*th observation and $\langle I_i \rangle$ is the mean intensity of the reflection.
[b] $R_{work} = \sum(||F_{obs}| - |F_{calc}|| / \sum|F_{obs}|)$
[c] R_{free} = R value for a randomly selected subset (5%) of the data that were not used for minimization of the crystallographic residual.
Highest resolution shell is shown in parenthesis.

Table S2 – Yeast strains used in this study.

Strain	Genotype
YS221	MATa*nup145::KANMX4 NUP133-GFP:HIS3MX6 met17Δ0 leu2Δ0 his3Δ1 ura3Δ0* [SBYp116;(*NUP145, LEU2, CEN)*]
YS222	MATα*nup145::KANMX4 NUP133-GFP:HIS3MX6 met17Δ0 leu2Δ0 his3Δ1 ura3Δ0* [SBYp117; (*nup145C-ELIEA, LEU2, CEN)*]
YS223	MATα*nup145::KANMX4 NUP84-GFP:HIS3MX6 met17Δ0 leu2Δ0 his3Δ1 ura3Δ0* [SBYp116; (*NUP145, LEU2, CEN)*]
YS224	MATα*nup145::KANMX4 NUP84-GFP:HIS3MX6 met17Δ0 leu2Δ0 his3Δ1 ura3Δ0* [SBYp117; (*nup145-ELIEA, LEU2, CEN)*]
YS225	MATα*nup145::KANMX4 met17Δ0 leu2Δ0 his3Δ1 ura3Δ0* [SBYp115;(*NUP145, URA3, CEN)*]

Correction: 28 November 2008

Supporting References:

1. S. Doublie, *Methods Enzymol* **276**, 523 (1997).
2. Z. Otwinowski, W. Minor, *Methods Enzymol* **276**, 307 (1997).
3. G. M. Sheldrick, *Acta Crystallogr A* **64**, 112 (2008).
4. P. D. Adams *et al.*, *Acta Crystallogr D* **58**, 1948 (2002).
5. P. Emsley, K. Cowtan, *Acta Crystallogr D* **60**, 2126 (2004).
6. A. T. Brunger *et al.*, *Acta Crystallogr D* **54**, 905 (1998).
7. B. DeLaBarre, A. T. Brunger, *Acta Crystallogr D* **62**, 923 (2006).
8. I. W. Davis *et al.*, *Nucleic Acids Res* **35**, W375 (2007).
9. P. Schuck, *Biophys J* **78**, 1606 (2000).
10. R. S. Sikorski, P. Hieter, *Genetics* **122**, 19 (1989).
11. C. Janke *et al.*, *Yeast* **21**, 947 (2004).
12. J. Garcia De La Torre, M. L. Huertas, B. Carrasco, *Biophys J* **78**, 719 (2000).
13. O. O'Sullivan, K. Suhre, C. Abergel, D. G. Higgins, C. Notredame, *J Mol Biol* **340**, 385 (2004).
14. M. Clamp, J. Cuff, S. M. Searle, G. J. Barton, *Bioinformatics* **20**, 426 (2004).
15. B. Rost, G. Yachdav, J. Liu, *Nucleic Acids Res* **32**, W321 (2004).
16. L. Holm, C. Sander, *Trends Biochem Sci* **20**, 478 (1995).
17. C. Notredame, D. G. Higgins, J. Heringa, *J Mol Biol* **302**, 205 (2000).
18. M. Lutzmann, R. Kunze, A. Buerer, U. Aebi, E. Hurt, *EMBO J.* **21**, 387 (2002).